Digital Comprehensive Summaries of Uppsala Dissertations
from the Faculty of Science and Technology 2293

Novel strategies to increase throughput and differentiate lipid isomers in mass spectrometry imaging

Development of computational tools and complex mass spectrometric methods for nanospray desorption electrospray ionization

JOHAN LILLJA

ACTA UNIVERSITATIS
UPSALIENSIS
2023

ISSN 1651-6214
ISBN 978-91-513-1870-7
urn:nbn:se:uu:diva-509042

UPPSALA
UNIVERSITET

Dissertation presented at Uppsala University to be publicly examined in Room A1:107a, BMC, Husargatan 3, Uppsala, Friday, 29 September 2023 at 09:00 for the degree of Doctor of Philosophy. The examination will be conducted in English. Faculty examiner: Professor Orešič Matej (Örebro Universitet).

Abstract
Lillja, J. 2023. Novel strategies to increase throughput and differentiate lipid isomers in mass spectrometry imaging. Development of computational tools and complex mass spectrometric methods for nanospray desorption electrospray ionization. *Digital Comprehensive Summaries of Uppsala Dissertations from the Faculty of Science and Technology* 2293. 60 pp. Uppsala: Acta Universitatis Upsaliensis. ISBN 978-91-513-1870-7.

In this thesis, method development for improved analyte identification and throughput in mass spectrometry imaging (MSI) is discussed. In MSI, the spatial distribution of analytes from a sample is determined and visualized, information about the detected molecules interaction within the sample can thereby the deduced. Most MSI methods utilize high resolution accurate mass (HRAM) to assign an identity to a feature by its mass-to-charge (m/z) value. However, HRAM cannot distinguish isomeric species. I have therefore developed novel tools for annotation and separation of lipid isomer for MSI with nanospray desorption electrospray ionization (nano-DESI). Specifically, I show that tandem mass spectrometry (MSn) of silver ion species of lipids can be used for the separation of both fatty acid and phospholipid isomers.

Additionally, I developed a method for parallelized MSn experiments, by performing multiple ion trap MSn in parallel to a fourier transform mass spectrometry (FTMS) transient. The ion trap MSn, albeit with lower resolution, has orthogonal specificity to FTMS and therefore generates a data set where the analytes identity can be deduced. Because the ITMS is executed in parallel to the typically used FTMS scan the imaging parameters are kept constant, thus generating a richer data set without increasing spatial resolution or experimental runtime.

Lastly, data sets generated with nano-DESI MSI are complex and require specialized software tools for processing. I also discuss an open-source tool for data processing with high flexibility and fast processing speeds. With the newly developed tool we were able to process and interrogate data sets, thereby making better use of the acquired data.

Keywords: Mass spectrometry, Mass spectrometry imaging, Tandem mass spectrometry, Silver cationization, Mathematical modeling, Lipid, Lipid isomer

Johan Lillja, Department of Chemistry - BMC, Analytical Chemistry, Box 599, Uppsala University, SE-75124 Uppsala, Sweden.

ISSN 1651-6214
ISBN 978-91-513-1870-7
URN urn:nbn:se:uu:diva-509042 (http://urn.kb.se/resolve?urn=urn:nbn:se:uu:diva-509042)

To my family

List of papers

This thesis is based on the following papers, which are referred to in the text by their Roman numerals.

I **Lillja, J.**, Duncan, K.D., and Lanekoff, I., Determination of Monounsaturated Fatty Acid Isomers in Biological Systems by Modeling MS^3 Product Ion Patterns, Journal of the American Society for Mass Spectrometry 2020 31 (12), 2479-2487

II **Lillja, J.**, Lanekoff, I. Quantitative determination of sn-positional phospholipid isomers in MS^n using silver cationization. Analytical and Bioanalytical Chemistry 414, 7473-7482 (2022).

III **Lillja, J.**, Lanekoff, I., Correlative image analysis for in-depth chemical analysis using multiple parallelized mass spectrometry imaging with high resolution and MS^n, (Manuscript)

IV **Lillja, J.**, Duncan, K.D., and Lanekoff, I., Ion-to-image, i2i, a mass spectrometry imaging data analysis platform for continuous ionization techniques, Analytical Chemistry 2023 95 (31), 11589-11595

Contribution report

The author would like to clarify his contributions to the research presented in papers I-IV.

I Conceptualization, performed experiments, developed methodology, made figures, wrote the original draft of the manuscript, helped in finalizing the manuscript

II Conceptualization, performed experiments, developed methodology, made figures, wrote the original draft of the manuscript, helped in finalizing the manuscript

III Conceptualization, performed experiments, developed methodology, made figures, wrote the original draft of the manuscript, helped in finalizing the manuscript

IV Performed experiments, developed methodology, made figures, wrote the original draft of the manuscript, helped in finalizing the manuscript

Contents

1. Introduction

There are three fundamental questions in analytical chemistry, what are we measuring, how much are we measuring, and where is it from? In this thesis, I will discuss the methods that I have developed to answer these questions with mass spectrometry imaging (MSI). Contrary to traditional workflows, in mass spectrometry imaging the sample is not digested in bulk, but precisely sampled from specific locations on its surface and reconstructed to an image. Because mass spectrometry is a structurally sensitive detector, complex samples can be measured and the localization of molecules across a sample surface can be determined both qualitatively and quantitatively. It is therefore a powerful workflow for answering all three fundamental questions.

However, with minimal sample preparation and separation – contrary to chromatography-based workflows – specificity and sensitivity is lost. Therefore, there is a need to develop methods that can give the desired specificity and sensitivity in other ways. In this thesis, I will describe and discuss the use of high-resolution accurate mass spectrometry (HRAM-MS), tandem mass spectrometry (MS^n), and computational methods to increase specificity, sensitivity, and throughput.

In **papers I and II** isomers of different lipids are measured with MS^n methods and mathematical modeling. **Paper III** describes a method that combines a targeted and a non-targeted mass spectrometry workflow for improved annotation and better signal quality. Lastly, in **paper IV** a novel computational tool was developed for ion image generation and data analysis of MSI data, for increased throughput and aid for non-targeted data exploration.

2. Mass spectrometry

At the forefront of this work is mass spectrometry. Mass spectrometry is a technique in which the mass-to-charge ratio (*m/z*) of ions is determined by manipulating the trajectory of an ion in an electromagnetic field. By either steering the ion(s) to a detector or recording the ion(s) trajectory the mass-to-charge ratio can be determined, from which the identity of the ion may be deduced.

The power of an *unbiased* (molecules still need to be ionizable) and structurally sensitive detector has driven developments in analytical chemistry and MS-based instrumentation very fast. However, mass spectrometry is still a relatively new technique, and there are many nuances of mass spectrometry that need to be considered for a successful experiment, such as ionization technique/ionizability of the analyte, dynamic range, ion transmission, specificity of the measurement, and selectivity of the measurement. In this chapter, I will describe some background and important concepts for my work with mass spectrometry.

2.1 Ionization

The first problem to overcome for bioanalytical mass spectrometry is how to generate intact ions of the analytes. In the early days of mass spectrometry, the harsh ionization techniques used limited the use of mass spectrometry for bioanalytical applications because the high energies needed for ionization caused the molecules to fragment. [1]

However, with the advent of matrix-assisted laser desorption (MALDI) and electrospray ionization (ESI) molecules could be ionized with minimal fragmentation and thus enabled mass spectrometry for the study of biomolecules.[2, 3]

The work in this thesis relies on electrospray ionization which is illustrated in Figure 2.1. In the ESI process, the sample containing liquid is made into a fine mist by the action of an applied electric field between an emitter and the mass spectrometer inlet.[4] Depending on the size of the emitter, the solvent used, and the electric field strength this initially produces charged droplets between 1-10 μm in diameter.[5] As the initial droplets travel toward the inlet of the mass spectrometer solvent continuously evaporates. As the droplet shrinks, the electrostatic repulsion within a droplet increases. Eventually, the electrostatic repulsion within the droplet becomes too high, and the droplet

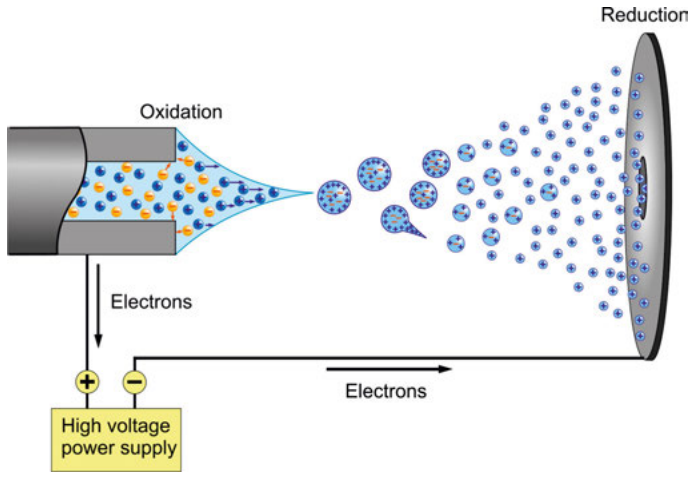

Figure 2.1. Illustration of positive mode electrospray ionization. Illustrated by and copyright Andreas Dahlin, https://flickr.com/photos/136533650@N02/21589986840, the illustration has not been altered in any way, confirmed to be under cc-by-2.0

explodes, which is called the Rayleigh limit. The evaporation and *explosion* process repeats and eventually forms solvent-free ions in the gas phase. There are several models that describe how ions are actually formed with electrospray ionization, the ion ejection model (IEM), charged residue model (CRM), and the chain ejection model (CEM).[6–8] The IEM model can be used to describe the ion formation of smaller ions, whereas the CRM and CEM models have been shown to explain the ionization process for proteins, peptides, and polymers.

In commercially available ESI sources, evaporation of the droplets – and thereby the ionization – is enhanced by the incorporation of heaters and nebulizing gases. Additionally, a lower flow rate and a smaller ESI emitter also generate smaller droplets and thus allow more efficient ionization. There is a special case of ESI, nano-ESI, where the efficiency of ionization is much greater than regular ESI. It occurs when the flow rate is below 50 $nLmin^{-1}$.[9]

2.1.1 Silver cation formation

The ions that can be generated with ESI are dependent on how a charge can be attached to the molecule. For example, nitrogen-containing compounds can easily oxidize and attach a proton under the conditions in positive mode ESI, and carboxylic species readily lose a proton and form an anion in negative mode ESI. Analytes may also form adducts, which in bioanalytical mass spectrometry is often seen in the positive ion mode as the complexation between an alkali metal ion and an electronegative site on the analyte. ESI thereby ex-

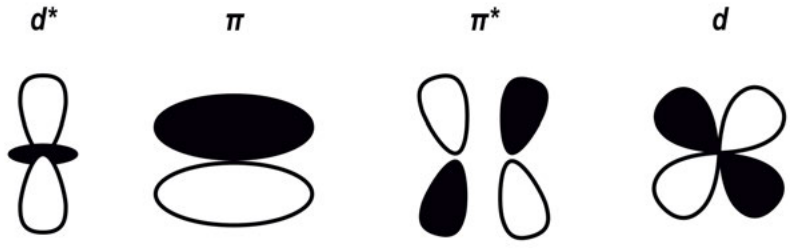

Figure 2.2. Visualization of d atomic orbitals and π molecular orbitals, * notes the lowest unoccupied level

cludes a large number of molecules that don't have readily ionizable functional groups or electrostatic hot spots.

Fundamentally for the work in **papers I, II, and III**, silver was used as an ionization reagent. The d-orbitals of a silver ion may form a bond with π molecular orbitals because of the complementing symmetry of d^*/π and d/π^* generates a Ag^+–M complex, illustrated in figure 2.2.[10] Silver adduct species of fatty acids and prostaglandins measured in the positive ion mode have been shown to increase the sensitivity for the analysis by at least an order of magnitude compared to the negative ion mode.[11, 12] The sensitivity increase combined with enabling novel fragmentation pathways was leveraged in **papers I and II** to deduce the isomeric composition.

Additionally, silver has a very recognizable isotopic pattern of 51.8/49.1 % of ^{107}Ag and ^{109}Ag respectively.[13] The isotopic pattern was used in the method development stage for **papers I and II** by confirming the presence of both isotopes on the target analyte. However, the presence of both silver isotopes creates a spectral interference between $[M+^{107}Ag]^+$ and $[M+^{109}Ag - H_2]^+$, which complicates its use in complex matrices. For measurements in complex matrices, such as in **papers I, II, and III**, I used monoisotopic ^{107}Ag to remove this interference. Additionally, by not diluting the signal into an additional isotopologue, the sensitivity is increased by the use of monoisotopic silver.

2.2 Ion trap mass spectrometry

Once ions are formed, they can be manipulated in electric or magnetic fields to separate according to their mass-to-charge ratio. In this work, I have been utilizing ion trap mass spectrometers.[14] In an ion trap, a population of ions is captured and manipulated to be ejected or resonate at different frequencies to be detected.

In ion trap mass spectrometry, it is especially important to control the size of the measured ion population. Too few ions do not generate a *good enough* sig-

nal and low dynamic range, and too many ions generate space-charge effects, which results in poor spectral quality.

To combat this there is a set time in which the ion current is sampled, thus controlling the size of the the population with the injection time. However, in chromatographic and mass spectrometry imaging applications the incoming ion current is variable in time. There is therefore not a one size fits all injection time to maximize sensitivity and accuracy.

The instruments I have been working with have a feature called automatic gain control (AGC), which works by performing a fast pre-scan to estimate the incoming ion flux.[15] By calculating the incoming ion flux the injection time can dynamically be adjusted to reach a given number of ions (or charges) in the device. Thereby maximizing the sensitivity, precision, and dynamic range at all times.

One of the biggest drawbacks of trapping mass analyzers is the limited ion population measured in each scan, and the lower utilization of the ion current compared to beam-type instruments. For mass spectrometry imaging applications, it is important to realize the limitation so experiments can be designed appropriately. For example, an experiment in an ion trap may be run in a limited mass range to increase sensitivity.[12]

Another important parameter in MSI is mass resolving power and duty cycle. Because the ionization is performed on a large mixture of analytes, MSI experiments are especially susceptible to isobaric interferences. High mass resolving power is therefore needed to reduce the number of spectral interferences. The mass resolving power is defined as $\frac{M}{\Delta M}$ where ΔM is the peak width at a specified peak height (typically 50 %) and is a quantitative metric of an instrument's ability to separate two neighboring peaks.[16] Additionally, since tens of thousands of spectra are needed to construct an ion image, the speed at which the mass spectrometer can generate sufficient mass-resolving power is also important.

2.2.1 Linear ion trap

One kind of mass analyzer that has been utilized in this work is the linear ion trap, or specifically a dual linear ion trap. A linear ion trap is different from a traditional paul ion trap, where the linear geometry allows for a larger charge capacity thus increasing the sensitivity and/or dynamic range of the mass analyzer.[17] The speed at which an ion trap can scan is determined by the mass range and the bandwidth of the applied ejection frequency. With the analyzers I have worked with the scan speed ranges from 66,666 *m/z*/s at FWHM ≤ 0.6 to 2200 *m/z*/s at FWHM ≤ 0.3. Commonly, the detector system is an electron multiplier detector that provides high sensitivity and broad dynamic range.[18]

To efficiently trap ions in an ion trap there is a need for a background gas to which the incoming ions can transfer the excess kinetic energy. However, the

ejection of ions at higher gas pressures reduces the scan rate due to less efficient energy transfer, because of energy transfer to the background gas. A dual linear ion trap setup where a high-pressure trap is put in series with a low-pressure trap can therefore scan at higher rates, illustrated in Figure 2.3.[19] In this way, the incoming ion current can be efficiently trapped before being sent to the faster mass-analyzing low-pressure ion trap. Additionally, this architecture also increases the ion current utilization by being able to prepare an ion package for measurement at the same time as the low-pressure ion trap generates a spectrum.

Linear ion traps are also capable of multi-stage isolation and activation of ions, thus enabling complex tandem mass spectrometry methods (MS^n) to be executed. This capability was leveraged in both **papers I and II** to generate structurally informative product ions.

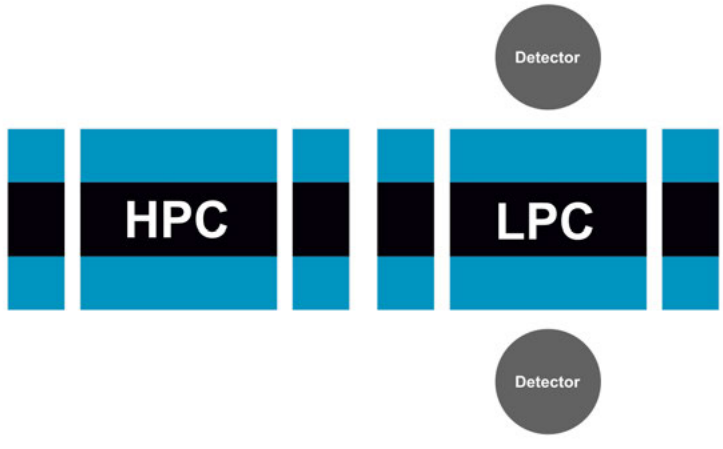

Figure 2.3. Illustration of a dual linear ion trap with a high-pressure cell (HPC) and a low-pressure cell (LPC). Adapted with permission from Pekar Second, T. et al. *Analytical Chemistry* **2009**, *81*, 7757–7765 ©2009 American Chemical Society

2.2.2 Orbitrap FTMS

Another mass analyzer that enabled this work was the high-resolution-accurate-mass Orbitrap mass analyzer. In 1999 a small company from the UK introduced the Orbitrap mass analyzer to the world, which utilized an electrical field for *m/z* determination with Fourier transform mass spectrometry (FTMS) instead of magnetic fields as otherwise commonly used.[20] This innovation enabled FTMS to be done with less complex instrumentation, at lower costs, and at greater speeds than ever before. The Orbitrap has been subject to fast technological developments since its inception and was commercially avail-

able five years after its proof of concept, and continuously developed with improved Orbitrap mass analyzer and different hybrid architectures.[21–25]

The specific geometry of the Orbitrap generates an electric field (U) as described in equation 2.1 that allows ions to oscillate in the trap along the z axis with a frequency inversely proportional to its *m/z* value (Equation 2.2), as illustrated in Figure 2.4. [21] Where r and z are cylindrical coordinates, k a constant, and R_m the characteristic radius.

$$U(r,z) = \frac{k}{2}\left(\frac{z^2 - r^2}{2} + R_m^2 ln\frac{r}{R_m}\right) \tag{2.1}$$

$$\omega_z \propto \sqrt{\frac{k}{m/z}} \tag{2.2}$$

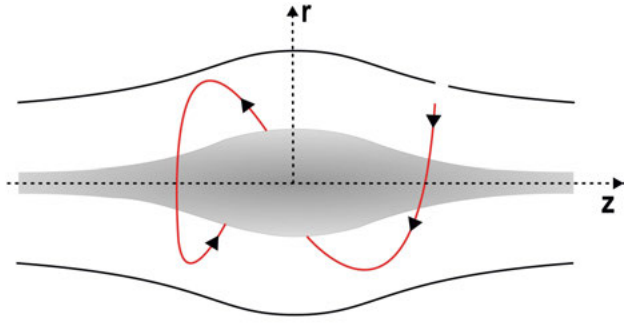

Figure 2.4. Illustration of an Orbitrap mass analyzer with commonly used axis notation. The orbit of an ion injected through the slit in the top electrode is also shown with the red line. Adapted from Makarov, A. *Analytical Chemistry* **2000**, *72*, 1156–1162 ©2000 American Chemical Society

The oscillating ions are detected by image current detection in the outer electrodes, and the frequency of the electrical signal is processed by Fourier transformation (FT) to construct a mass spectrum. As with any FTMS mass analyzer, a higher mass resolving power is achieved with a longer recorded transient. A standard Orbitrap is capped at 1 or 1.5 seconds, but ions can be stable, and ultra-high mass resolution has been shown with longer transients.[26, 27] There are two main methods of FT processing, magnitude mode, and absorption mode.[28] In magnitude mode processing the magnitude of the signal is used, whereas in absorption mode the phase of the signal is also taken into account. By accounting for the phase of the signal the mass resolving power can be increased by a factor of two, however, this also introduces spectral artifacts that may be undesirable.[29, 30]

In modern Orbitrap instruments, a proprietary enhanced Fourier transform (eFT) is used to attain high mass resolving power but with fewer spectral artifacts. This is done by combining magnitude mode and absorption mode processing, by effectively using absorption mode for the top half of the peak and

magnitude mode for the bottom half of the peak.[30] Thus generating spectra without artifacts at high mass resolving power in a relatively short period of time.

As with any trapping mass analyzer, there may be detrimental space charge effects that can ruin an experiment. In particular, for FTMS examples of detrimental space charge effects are ion coalescence, self-bunching, and signal decay. [31–33] The first two are synchronization phenomena where ion clouds with similar frequencies start to resonate with the same frequency. This causes closely spaced *m/z*-packages to be detected with the same frequency thus losing mass resolving power. Self-bunching is the effect where the ions in the same ion cloud bunch together and produce a narrower frequency distribution than what should be possible, which may seem like a good thing, however, peaks in its vicinity will be coalesced and not detected.[32] Additionally, the ion decay rate in the trap is non-linear, and low abundant ions decay at a different rate to highly abundant ones, thereby making accurate ratiometric measurements between two peaks at different intensities very difficult.[33] The space charge effects are quite efficiently minimized by AGC and other features making the Orbitrap a relatively user-friendly high-end mass spectrometer. However, for specialized applications such as MSI expert users are still needed to maximize the performance of the instrument.

Throughout my work, I have used several hybrid architectures of Orbitrap mass spectrometers, the Orbitrap Velos Pro which is an IT-Orbitrap hybrid, and the Orbitrap IQ-X which is a Q-IT-Orbitrap hybrid.[22, 25] The ion trap allows for measurements of the ion current, isolation of specific *m/z*-ranges, MS^n experiments, and orthogonal detection to the Orbitrap mass analyzer – thus making the instrument extremely versatile. In the Q-IT-Orbitrap, a quadrupole mass analyzer is installed after the first ion optics, allowing quadrupolar isolation of specific *m/z* values which increases speed and sensitivity in complex mass spectrometry experiments. Since the quality of the data of trapping instruments is directly determined by how many ions you measure, controlling the ion population entering the trap with a quadrupole increases sensitivity since space in the trap is not occupied by ions that are not of interest for that specific experiment. Specifically, in **paper III** I leverage the quadrupole isolation to generate high-quality MS^2 data of lipids in parallel to the FTMS transient, enabling parallel detection of 28 MS^2 transitions.

2.3 Tandem mass spectrometry

To get even greater insights into what is actually measured in a mass spectrometer, tandem mass spectrometry experiments (MS^n or MS/MS) can be performed. In an MS^n experiment, schematically shown in eq. 2.3, the complex AB^+ is activated to a metastable state AB^{+*} which dissociate to the ion A^+ and B. [34]

$$AB^+ \rightarrow AB^{+*} \rightarrow A^+ + B \tag{2.3}$$

There is a multitude of ways to increase the internal energy of ions in the gas phase, such as; collision-induced dissociation, ultraviolet photodissociation, electron capture and electron transfer, and infrared multiphoton dissociation to name a few, which are different in how the energy is supplied to the ion and what kind of product ions are to be expected.[35–39]

I have worked with collision-induced dissociation (CID), which is a standard feature on almost all modern mass spectrometers. In ion trap CID, a resonant frequency is applied to an isolated ion package increasing its kinetic energy. Ion trap CID is a specific subclass of CID methods, where the energy is *slowly* increased in the ions over several milliseconds.[40] The excited ions collide with a background gas and the internal energy of the selected ion is increased. Once enough energy has been applied the ion(s) dissociate and form product ions. Because of the *slow* heating of the ions, it is most likely that dissociation pathways with low activation energies are observed in the product ion spectrum.[41] Although this generally makes ion trap CID have high yields and good repeatability, it may pose a challenge for specificity because less specific dissociations tend to dominate the spectrum.[34, 42]

In **papers I and II** ion trap CID was used to generate structurally informative product ions by exploring dissociation pathways enabled by silver adducts. Because the silver adduct localizes to π moieties, which is different from otherwise commonly used adduct species such as H^+, Na^+, and K^+ reactive and unique intermediate product ions was formed and could be studied in MS^n.

The localization of the silver ion to π moieties allowed for multi-stage MS^n of fatty acids and glycerolipids. This allowed for less informative functional groups such as the carboxylic acid moiety in the case of the fatty acid, and the modified phosphate moiety for the glycerophospholipid, to be removed at an early stage of MS^n. These functional group generally carries the charge of the ion, and when removed disqualifies the products to be studied further. The localization of the silver ion at π moieties allowed less informative functional groups to be removed from the isolated ion(s) in the early stages of MS^n. Further activation of the product ions to MS^3 or MS^4 therefore allowed for structurally informative product ions to be formed.

2.4 Ion mobility spectrometry

Ion mobility spectrometry (IMS) is a technique where ions are separated based on the collisional cross section (CCS) and can be very powerful in the analysis of complex mixtures when coupled with mass spectrometry. The principle upon all IMS methods rely upon is the retardation of ions in an electric field in the presence of a background gas, where ions with a larger surface area will traverse the IMS device slower compared to an ion with a smaller surface area. There are many different ways IMS can be done, such as drift tube, trapped ion mobility, traveling wave, field asymetric ion mobility spectrometry, and differential ion mobility.[43] In IMS, the CCS resolving power is proportional to the length of the device. In **paper II** we used a cyclic traveling wave ion mobility device (cTWIM), which can reach effective lengths of several meters by circling the ions in the cyclic device. Ion mobility resolutions of about 750 ($\frac{CCS}{\Delta CCS}$) have been shown with 100 passes in cTWIM devices.[44]

A unique feature of a cTWIM device is that it can in addition to CCS measurements also perform tandem ion mobility (IMS^n) experiments. IMS^n is similar to MS^n experiments, but precursor ions are isolated based on their drift time rather than its *m/z* value. Due to the architecture of the device, product ions can be sent back into the cTWIM device and separated again, thus enabling IMS^n. In this way, not only are the mass-to-charge value of the product ions deduced, but also their respective CCS. In **paper II** we utilized cTWIM to study the dissociation of regioisomers of phospholipids. It has previously been shown that phospholipid regioisomers can be separated with ion mobility as $M–Ag^+$ ions, and we show that product ions containing Ag^+ are also separable through IMS.[45] However, when the silver ion was lost, the ions were inseparable by IMS^n, which could explain the quantitative nature of the developed method where ions of both the same elemental composition and structure should dissociate similarly.

3. Mass spectrometry imaging

The question *where is a molecule located in the sample?* can be answered in many different ways. One type of experiment that can answer this question is mass spectrometry imaging (MSI), which is the focus in this thesis. Although first demonstrated with secondary ion mass spectrometry (SIMS) for inorganic samples in 1962 by Castaing and Slodzian, bioanalytical MSI was first shown in 1994 by B. Spengler, and first published in 1997 by R. Caprioli utilizing a much softer MALDI ion source.[46–48]

In a MSI experiment, a portion of a sample from known locations is ionized and detected with a mass spectrometer. Because the location in which each mass spectrum was acquired is known the spectra can be reconstructed to an image, where each *pixel* corresponds to the mass spectrum from that specific location. The distribution of the different *m/z* values detected can thus be deduced, revealing the localization of specific analytes in the sample. The MSI methodology has allowed for detailed studies of biochemical processes in tissue to aid in understanding diseases such as ischemic stroke, diabetes, and cancer.[49–51]

Today, there are many different techniques available for bioanalytical MSI which include; SIMS, ambient pressure MALDI (AP-MALDI), desorption electrospray ionization (DESI), and nanospray desorption electrospray ionization (nano-DESI) to name a few.[52–55] All of these have their specific strengths and weaknesses. For example, SIMS may be used for extremely high spatial resolution but is limited in analyte coverage. MALDI experiments may also have good spatial resolution and are excellent for peptides and lipids, but it can be challenging to separate low molecular weight compounds from matrix peaks. DESI is done with little sample preparation and can measure small metabolites, but reproducibility and spatial resolution has traditionally been limiting it. nano-DESI is also done with little sample preparation, and it is easy to compensate for matrix effects by internal standard normalization, but requires highly trained users to operate and has relatively long analysis time.

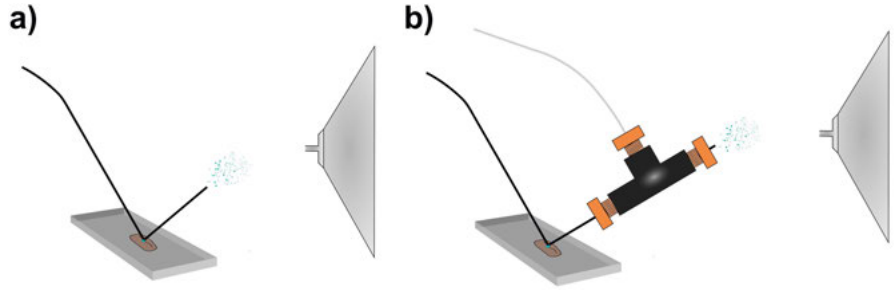

Figure 3.1. Illustration of the nano-DESI (a) and PA nano-DESI set up (b). The high voltage is applied at the syringe supplying liquid in the non-spraying capillary.

3.1 nano-DESI MSI

In this work, I have utilized nano-DESI MSI. Nano-DESI is a relatively recent technique and was invented in 2010 at the Pacific Northwestern National Laboratory in Washington USA.[55]

The setup of a nano-DESI probe is illustrated in Figure 3.1 a), where a primary capillary supplies solvent to the surface, and the secondary capillary aspirates the solvent and ionizes the extracted material from the liquid junction between the two. A sample is placed on a regular microscope slide and placed on a computer-controlled XYZ-stage which is programmed to move in a rasterization pattern across the sample, thus being able to do MSI.[56]

The motivation to develop this technique was to increase the number of ions reaching the mass analyzer and to decouple the desorption and ionization events by implementing a secondary capillary to a traditional DESI setup.[55] The number of ions entering the mass spectrometer is high for nano-DESI, where millions of ions are generated and sent to the mass analyzer, which can be compared to tens of thousands in a publicly available AP-MALDI data set (Figure 3.2). The high ion yields allow for sensitive detection and MS^n experiments, as expanded upon in **papers I, II, and III**.[58]

Furthermore, because the desorption event and ionization events are decoupled, addition(s) of internal standard(s) allows for unbiased image normalization and quantitative interpretation of the resulting ion images.[59] Image normalization is imperative in MSI, because the ion images may be influenced by matrix effects.[59, 60] The effect of internal standard normalization is shown in Figure 3.3, where the raw and total ion current normalized ion image shows a homogenous distribution, whereas the internal standard normalized ion image shows clear histological features. This highlights that the use of internal standard(s) for nano-DESI MSI is necessary, and totally opposite biological conclusions may be drawn if appropriate normalization is not done. Furthermore, by using an internal standard it is also possible to quantify the desorbed material and generate quantitative ion images for greater insights.

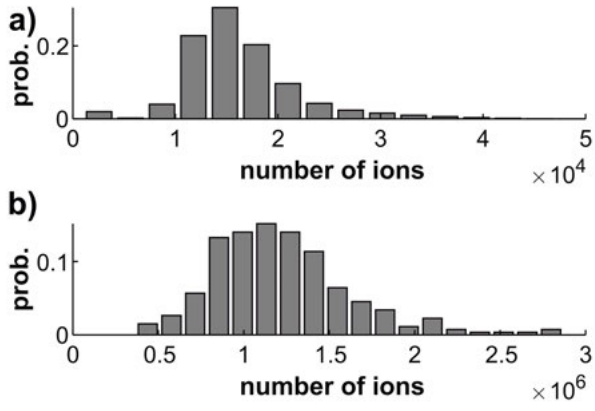

Figure 3.2. The flux of ions per scan in a) AP-MALDI (public data available from ref.[57] and b) nano-DESI MSI. The nano-DESI MSI generates about two orders of magnitude more ions compared to the AP-MALDI.

With any MSI technique, one important factor to consider is the spatial resolution it is capable of. Especially since it defines what histological features that may be detected in a sample. Throughout this work, I use the estimated pixel size, which in nano-DESI MSI is different in width and height. The width of each pixel is determined by the sampling rate of the mass spectrometer and the velocity at which the sample is moved. If for example the velocity is 20 μms^{-1} and the scan rate is 1 Hz, each pixel is 20 μm wide. The scan rate and sample movement velocity can be chosen to get the desired pixel size in the sampling direction. The height of the pixel is estimated by the size of the liquid junction and is approximated by the size of the capillaries, which throughout my work has been 150 μm. The height of the pixel can be lowered by oversampling, which is done by *overlapping* the rasterization lines to reduce the pixel height.[61] Additionally, smaller capillaries can be used to make the footprint of the droplet smaller. However, with a smaller droplet the distance between the surface and the liquid junction becomes increasingly sensitive to fluctuations. In the group of Prof. Julia Laskin at Purdue University, USA, a shear force probe was developed to measure the distance between the liquid junction and the sample surface, and with a feedback mechanism adjust the distance as necessary.[62] By dynamically adjusting the distance they were able to resolve 10 μm features in mouse brain.

To me, the biggest benefit of nano-DESI is to me the high ion yields, large analyte coverage, and flexibility to change/modify the solvent. Allowing for a vast array of experiments to be carried out, such as; shotgun lipidomics, imaging of small metabolites, and even native proteins.[63–65] **Papers I, II, and III** utilize the high ion yields from the combination of silver ions added to the

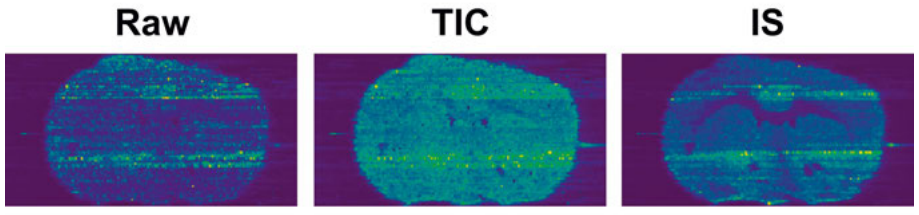

Figure 3.3. Raw, total ion current (TIC), and internal standard (IS) normalized ion image of *m/z* 866.4822 (PC 34:1+^{107}Ag) in a mouse brain section. All images are scaled to the 99th percentile of the pixel intensity values. The raw and TIC normalized ion images do not reveal the same features as the IS normalized, showing that matrix effects may mislead the interpretation of raw or improperly normalized ion images.

solvent and nano-DESI MSI to do both deep MS^n studies and broad MS^2 for improved annotation of lipid species.

3.1.1 pneumatically assised nano-DESI

A development of nano-DESI was presented in 2017, the pneumatically assisted nano-DESI (PA nano-DESI).[66] In PA nano-DESI, the secondary capillary is sealed tight in one end and loosely in the other in a tee-union connected to a gas source (Figure 3.1 b). The flow of gas around the tip of the secondary capillary causes a low-pressure zone just around the orifice of the capillary due to the Venturi effect, which aspirates the liquid. Because the aspiration of the solvent is dependent on the physicochemical properties of the solvent and the physical dimensions of the secondary capillary, the ability to adjust the flow through the secondary capillary by changing the supplied gas pressure is very convenient.[66] Additionally, the desolvation of the charged droplets from the ESI source is also aided by the flow of gas. In **papers I, II, and III**, the PA nano-DESI have been used for its increased ease of use and ruggedness.

3.2 Data processing

It is not trivial to generate ion images from MSI data sets, because of the large volume of data and metadata. There are commercial and open-source solutions available to the MSI community to generate ion images and to analyze data.[56, 67–70] However, because of the unique structure of the acquired data and the ability to perform complex MS experiments with nano-DESI cannot be processed with most currently available software solutions.

First, almost all programs assume that each pixel has exactly the same dimensions and arranges the data in a matrix form, where the x, y coordinate in the matrix corresponds to the spatial location where the spectrum was obtained. For continuous MSI modalities, such as nano-DESI, the location where

the spectrum was obtained is determined by the velocity of the stage and the duty cycle of the MS. However, the duty cycle of the mass spectrometer varies because of the automatic gain control in the mass spectrometer used here. An obvious solution would be to turn off the AGC, however, in a nano-DESI MSI experiment the ion flux is dependent on where in the tissue the material was extracted from. Therefore, to gain similar dynamic range and spectral accuracy throughout the experiment it is necessary to use AGC. The different ion injection times can cause the individual line scans to misalign and even not contain an equal number of scan events, making it impossible to directly impute the data in a rectangular matrix. To properly visualize nano-DESI MSI data it is therefore necessary to align all spectra in time.[56] Because the dimension of each pixel is unique, and the number of pixels per line may be different, the new time axis needs to contain more elements than the original data. Throughout my work, a 20 times increase in discretization has been used for the time axis, meaning that the new time axis has 20 times more 'pixels' than the most number of spectra acquired per line. The intensity values are then interpolated on a new time axis from t_0 to $t_{max(all)}$ where $t_{max(all)}$ is the longest scan time for all line scans. The effect of misalignment due to a variable duty cycle is exemplified in Figure 3.4, showing that time alignment is imperative for generating ion images with nano-DESI MSI.

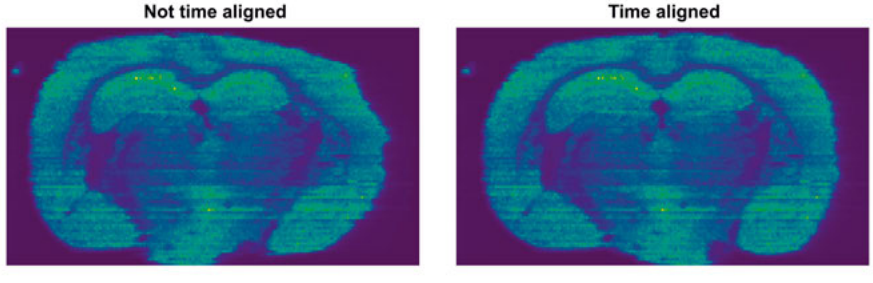

Figure 3.4. Ion image of PC 34:1 normalized to PC 25:0 showing distortion due to different ion injection times between pixels. The effect is visible by eye in the rightmost edge in the not time aligned ion image. Reprint from Lillja, J. et al. *Analytical Chemistry* **2023**, *95*, 11589–11595 ©2023 Author(s)

Secondly, the amount of ions produced makes it attractive to include many different MS experiments for the nano-DESI MSI data acquisition, as performed in **papers I, II, and III**. Where MS^n was performed along with typical full-MS scans to improve the specificity and/or sensitivity. To generate ion images from complex MS experiments containing an arbitrary amount of MS experiments is non-standard, and there was currently no available and simple solution for processing this kind of data. In **paper IV** we therefore developed a method to sort arbitrarily complex MSI data based on the *scan header*. The scan header is created by the mass spectrometer and is a string of metadata unique to the specific MS experiment. By sorting the data based on each

unique scan header we show that it was possible to easily and simply transition between different MS experiments within the same data set. Thereby greatly simplifying data processing of nano-DESI MSI data sets.

3.2.1 Data format

A MSI experiment generates a very large and rich data set, and generally generates around 1.5-4 GB of data for nano-DESI MSI with an Orbitrap mass spectrometer, but can reach several TB for full transient FT-ICR MSI experiments.[72] How the files are stored and accessed by the computer ultimately determines how the user can interact with the data and what can be learned from the experiment, in the sense that long and tedious data processing will not or can not be executed. It is therefore of the utmost importance that MSI data can be processed efficiently, so that as much as possible can be learned from an experiment. The raw data size is oftentimes the limiting factor for determining the processing time.

In the MSI community, there is an open file format most software applications can use, which is called .imzML.[73] Which is an extension of .mzML, with a specific file structure and metadata requirements for image reprocessing. However, the .imzML standard is strictly defined and requires a *square matrix* of pixels. This would either require AGC to be turned off, which would reduce the potential dynamic range or generate poor spectra, or to preprocess the data with the required interpolation making the file sizes huge. There is therefore a need for other solutions for the nano-DESI MSI data generated here.

In FTMS there are two levels of *raw* data, unreduced- and reduced data. An unreduced spectrum is either a non-processed transient or an absorption mode spectrum with the necessary metadata to reconstruct the transient. In this way, the spectrum can be reprocessed with for instance a different apodization or phase correction for improved spectral quality. However, unreduced data sets are large and are mainly used for research and specialized applications.

A more convenient data format is therefore the reduced data format, here, the data is compressed to such an extent that the original transient cannot be reconstructed and typically reducing the data size by a factor of 10.[74] In fact, the data generated from a regular Orbitrap FTMS measurement is stored in two reduced formats, profile, and centroid. The accurate mass is calculated from the profile data and saved in the centroid data stream in the .raw file. For the data processing methods described in **paper IV**, we work strictly with centroided data. Because the centroided data stream is already there, the only loss in information is how well the centroiding algorithm works. Specifically, the .raw files were converted to the open .XML based .mzML format as centroids.[75] By working in this reduced format we were able to load entire nano-DESI MSI data sets in the computer memory. The computer memory is about

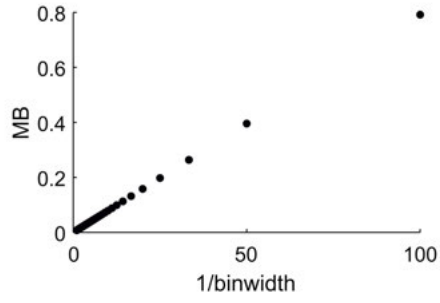

Figure 3.5. Memory needed to store a single array of bins between *m/z* 100-1000 as a function of bin width. The data was generated in MATLAB 2022a.

5-10 times faster than a modern solid-state drive, which enables fast queries to the data set. Thereby enabling the freedom to explore the entire data set.

3.2.2 Peak alignment

One obstacle in data processing of high-resolution accurate mass data is how to determine when two peaks are considered equal between spectra. This is important for the extraction of the correct peak in each spectrum to construct, in this case, an ion image. It is impossible to test the equality $m/z_1 = m/z_2$ between spectra because of both instrumental drift and the complexity of comparing floating point numbers. Therefore, spectral alignment needs to be done in other ways. One popular strategy is to use *binning*. When performing standard binning methods, a vector with n bins corresponding to a defined mass range is populated with the closest corresponding intensities. This can work well, however, there is a severe memory cost as the number of bins is increased (Figure 3.5). Additionally, because the bin represents a range of *m/z* values accurate mass information from the mass spectrometer is lost. Instead, we calculate the mass difference between a list of target ions and each spectrum using a parts-per-million (ppm) function as shown in Equation 3.1, where $\Delta m/z$ is the difference between the theoretical and detected *m/z*-value.

$$E_{ppm} = \frac{\Delta m/z}{m/z} \cdot 10^6 \tag{3.1}$$

In a nano-DESI MSI data set, the calculation of ppm mass accuracy needs to be executed on each ion searched for, for each spectrum, in the entire data set. Depending on mass resolving power and imaging parameters (line spacing and velocity) this results in 10 000 - 40 000 individual spectra, each containing thousands of peaks. Thus, a very large number of calculations are involved in solving this seemingly simple task. Specifically, in **paper IV**, I wrote fast vectorized code to calculate the closest *m/z* value in a spectrum compared to a

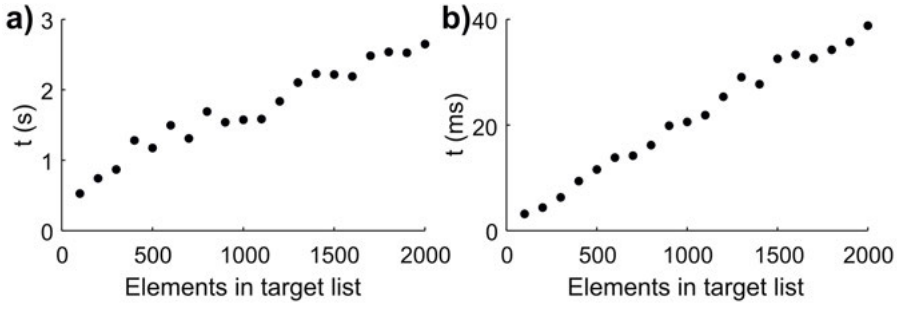

Figure 3.6. Time to find the n closest values in a 10000 elements large vector with MATLAB code for a) non-vectorized code and b) vectorized code. The vectorized code is two orders of magnitude faster.

target list, schematically described in Equation 3.2. In Equation 3.2 the variables *a* and *b* are vectors containing n and m target *m/z* values respectively, and *c* the matrix from their pairwise differences. The gain in performing computations on vectorized entities rather than sequentially is illustrated in Figure 3.6, with a two-order of magnitude increase in speed. Additionally, in the programing language used throughout this work, MATLAB, the created variable c is stored in a contiguous block of memory, making it possible to extract the desired values from the array extremely fast.

$$c_{n\times m} \leftarrow a_{n\times 1} - b_{1\times m} \tag{3.2}$$

There are drawbacks to how we executed this. Firstly, because variables are stored in contiguous blocks in memory in MATLAB making it fast, at the cost of beeing memory usage inefficient. Which may be a problem for larger data sets or if files get bigger in the future. Secondly, in cases where multiple *m/z* values are within the defined mass error, the code will pick the peak with the best mass accuracy. Meaning that if a noise peak arises that is very low abundant but has a better mass accuracy, will be chosen instead of the *real* peak. However, to some extent, the amount of noise and the signal-to-noise is user-defined parameters by the experimental parameters, and no peak-picking algorithm in the world compensates for low-quality data.

3.2.3 Non-targeted data analysis

Data sets generated with a MSI workflow are extremely rich, meaning that there is more information than what is relevant to the original hypothesis. Therefore, the data may be an excellent resource for generating new hypotheses to be studied later. However, performing spatially driven data exploration is not trivial. Because a MSI data set usually contains a lot of individual spectra, and each spectrum contains thousands of *m/z* values, spatially correlating these is

computationally expensive. Most methods rely on statistical analysis to group the *m/z* values in regions, taking anywhere from hours to minutes, depending on the data size and segmentation method used, on high-end workstations.[76]

In **paper IV** I developed a non-targeted analysis algorithm, which groups peaks in a defined area of the sample into peak groups that satisfy a mass accuracy tolerance. Here, an average spectrum is calculated in a defined region and compared to another region. By only considering spatial information in the first step the computations can be much quicker, and executed in real time. Although it does not define *new* regions like the unsupervised statistical methods, it can be used to quickly assess what features are detected in a given user-defined region.

The algorithm works by combining all *m/z* vectors in the defined area into a single array and sorted. The mass error between the element i and $i+1$ is then calculated, if the mass error is below the threshold a weighted average m/z_w is calculated between i and $i+1$ based on intensity and compared against element $i+2$, this process iterates until the mass accuracy tolerance is greater than the user-defined value. Once the ppm accuracy between m/z_w and $i+n$ is greater than the user-defined tolerance all values i to n are stored as a unique peak group and the algorithm starts over from $n+1$. The list of feature groups is then further processed based on the user-defined parameters; min/max intensity, and detection frequency. This way we can quickly generate a list of unique *m/z* values in the defined area. Additionally, a second region can be defined as a comparison region and used to find features that are unique or upregulated relative to the primary region. In this way, a complete MSI dataset can be quickly data mined and assessed in real-time. Thereby enabling greater utility of the data and aiding in generating hypotheses.

4. Spatial omics

Mass spectrometry-based -*omics* studies are powerful because the structurally sensitive detector allows the detection of all analytes with similar physicochemical properties from a sample in one experiment.[77–79] An -*omics* experiment can therefore be used to try to contextualize the interplay between different molecules within the sample, leading to a greater understanding of the underlying biological mechanisms.

There are two fundamental methods for -omics experiments, targeted and non-targeted.[80] In a targeted experiment a set of analytes is defined as interesting and internal standards are used to quantify each of the analytes. Whereas in a non-targeted experiment, the goal is to measure and quantify differences between as many analytes as possible between states (for example; sick/healthy, treated/untreated, region A/region B).

In this work, spatial -*omics* has been used, where the spatial distribution of the molecules in the sample is retained throughout the experiment. The analysis then compares different morphological regions in the sample or compares sick and healthy parts of the sample to make biological inferences. Two ways this can be done is by either micro-dissection of distinct features of a sample, or what I have worked with, MSI. [81–83] Herein, I will mainly focus on lipidomics – which is the study of lipids or a subclass of lipids in a sample.

4.1 Lipids

Lipids are one of the distinct classes of biomolecules and have many different functions. Lipids are used as structural elements in cell membranes, signaling molecules, and energy storage to name a few.[84] Here I have studied glycerolipids, glycerophospholipids, and fatty acids. Glycerolipids are a class of lipids that has functional groups bound to a glycerol backbone, as illustrated in Figure 4.1. This may form mono-, di-, tri- acyl glycerols if fatty acyl groups bind to the R_n sites, or phospholipids if the R_3 group binds to a modified or natural phosphate moiety, with a selection of R groups also shown in Figure 4.1. The different modifications lead to different physicochemical and biochemical properties, for instance, the curvature of a lipid membrane is dependent on the head groups, and the degree of unsaturation of the acyl chains affects the fluidity of a lipid bilayer.

There are a vast number of ways that lipids can be constructed, including different head groups, acyl chain length, unsaturation in the acyl chain, and which

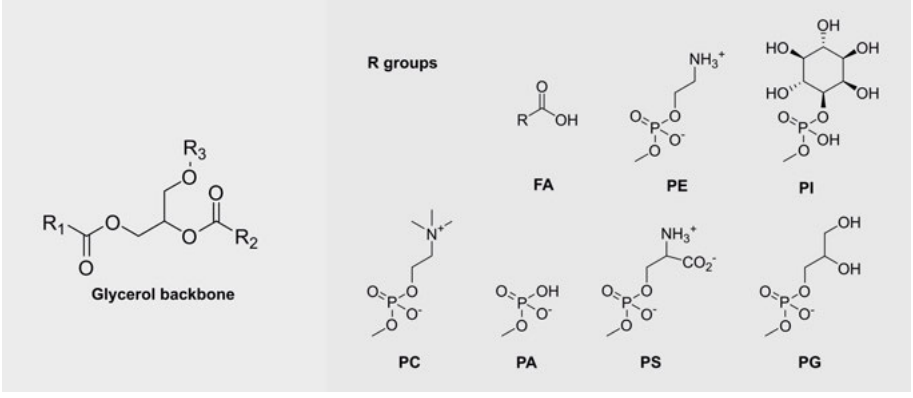

Figure 4.1. Glycerolipid diversity showing the glycerol backbone where R_1 is at the *sn-1* carbon, R_2 is at the *sn-2* carbon, and R_3 is at the *sn-3* carbon. By combining different headgroups at R_3 different phospholipids may be constructed. The selection of R groups shown here are; Fatty acids (FA), Phosphatidylethanolamine (PE), Phosphatidylinositol (PI), Phosphatidylcholine (PC), Phosphatic acid (PA), Phosphatidylserine (PS), and Phosphatidylglycerol (PG).

R group the acyl chain is bound to. Because of this, there is a specific shorthand naming scheme that has been developed and adapted for lipidomics.[85] Each lipid class has an abbreviated name, such as FA for fatty acid, PC for phosphatidylcholine, PA for phosphatic acid etc. The number of carbons and double bonds in the acyl chain is also abbreviated by either summing them all up to for example PC 36:1, for a PC lipid with a total of 36 carbons in the acyl chains and one double bond. If the acyl chain composition is known but the relative position is unknown the same lipid can be assigned PC 18:1_18:0, and lastly, if the relative position is known PC 18:1/18:0 where the first stated acyl chain means that it is attached to the sn-1 carbon.

Because of both the acyl chain position and double bond location, there are a lot of potential isomers that could be formed. For example, if there is an 18-carbon long unbranched acyl chain with two double bonds, combinatorics dictates that there are $\binom{18-1}{2}$ or 136 unique potential isomers. For a similar acyl chain but with three bonds, there are $\binom{18-1}{3}$, or 680 unique isomers etc. Additionally, the acyl chain may be bound to specific sites on a glycerol backbone, and have different double-bond stereochemistry, making the number of potential isomers extremely high. Thankfully, only a small subset of the potential isomers is usually detected in biological systems.[86, 87]

4.1.1 Identification

Mass spectrometry is a fantastic tool for the structural elucidation of lipids because of its ability to separate the analytes based on *m/z* rather than the analytes' physicochemical properties. Early lipid analysis was mainly utilizing normal phase or thin layer chromatography, which enables lipid class separation but struggles to separate lipids within the same class.[88] Although chromatographic separation of for example regioisomers is possible, it is mainly applicable for highly unsaturated acyl chains.[89] Developments in mass spectrometry based methods, using IMS or fragmentation strategies, are therefore imperative for the identification of the lipid species.[90]

The primary mode of identifying lipids is; *m/z*, accurate mass *m/z*-value, and product ions from MS^n experiments. Most lipids can be separated in the *m/z*-domain with modern high-resolution mass spectrometers, however, there are cases where extreme mass resolving power is needed and can complicate high-resolution accurate mass.[91] Specifically, the second ^{13}C-isotopologue of a lipid M is only 0.009 Th different from M with one less double bond. This small difference requires a mass resolving power between 65 000 and 100 000 to be resolved, but it is attainable on standard high-resolution mass spectrometers. However, there are also overlaps from different adduct species that can interfere. For PC species this can be seen between $[M+Na]^+$ and $[M+H+CH_2+3DB]^+$, which has a difference of 0.002 Th. Here, between *m/z* 600-1000 a mass resolving power of 300 000 to 500 000 is needed, which is currently not possible with a standard Orbitrap with a 1024 ms transient. But, it may be resolved with longer transient Orbitraps or high field FT-ICR.[27] Alternatively, tandem mass spectrometry strategies may be used to handle the aforementioned isobaric interference. In **papers II and III** I utilize monoisotopic silver as an ionization reagent and detect the analytes as $[M+^{107}Ag]^+$ for phospholipid analysis. Conveniently, these species do not form any isobaric interference thus facilitating simple data interpretation.

Novel lipidomic strategies

In the latest quest for insight, MS-based methods that can distinguish lipid isomerism are at the forefront. Previously unknown, or cumbersome to attain, attributes about lipid structure(s) are, with modern strategies, able to be deciphered. For example, there are lipid dysregulations at the double bond and *sn*-positional level in cancer.[92, 93]

There are a few different strategies that could be used in spatial lipidomic studies for elucidating the structure of lipids including; novel ion activation techniques, *exotic* adduct formation, and derivatization strategies.[94–96] To date, ultraviolet photodissociation (UVPD), electron induced dissociation (EID), ozone induced dissociation (OzID), charge inversion, and paterno-buchi (PB) has been used for this. [97–102] However, these strategies require modifications to the experimental set up that hinders the implementation in many labs.

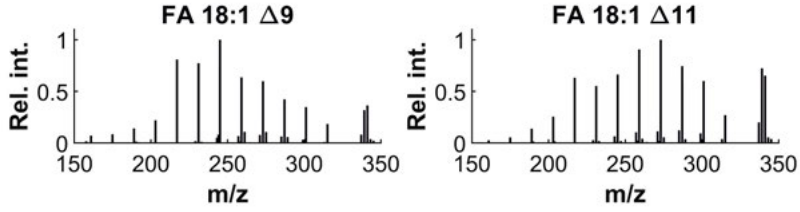

Figure 4.2. Product ion spectrum of oleic acid (left) and vaccenic acid (right) in MS^3 as silver adducts. The envelope of product ion peaks are different between the two isomers, but the product ions are the same. Adapted from Lillja, J. et al. *Journal of the American Society for Mass Spectrometry* **2020**, *31*, 2479–2487 ©2020 American Chemical Society

In **papers I and II** I studied how silver can be used to unravel the structure of lipids with MS^n, which is a standard feature in most ion trap mass spectrometers. Silver can in our case be added into the nano-DESI solvent and does not require any instrumental modifications and is therefore easy to implement. Because the silver ion has an affinity for π bonds, previously unexplored dissociation pathways could be explored. Because the silver ion retains the charge on the ion in MS^n the dissociation of the ions could be performed in several stages, with high sensitivity and specificity for complex mixtures.

In **paper I** I studied the dissociation pathway of fatty acid species as silver ion adducts in the positive ion mode. Silver chemistry has previously been shown to increase the sensitivity of fatty acid analysis.[11] However, to reveal the double bond position in complex mixtures further strategies had to be developed. Specifically, because the silver ion complexes around the double bond, structurally informative product ions with regard to the double bond position were formed in MS^3. At the MS^2 stage there is mainly loss of H_2O and an additional CO loss, which are not indicative of the double bond position. However, further fragmentation in MS^3 yielded a distribution of identical product ions, shown in Figure 4.2, that has different *center-of-mass* relative to where the double bond was located on the acyl chain.

Because the different isomers produce the same ions, but with different distributions, a modeling approach was used to determine mol % of the two isomers in mixtures. A stepwise multilinear model was employed in the regression, which is an iterative approach to model building where the dependent variables X in eq. 4.1 are tested for statistical significance at each iteration.[104] Here, I let the model freely add and remove dependent variables between iterations to find a model with the highest precision. The variable choices resulted in the algorithm choosing the 7 most intense product ions, and two interaction variables. This had good accuracy and was robust in complex matrices, the stepwise multilinear regression algorithm was, therefore, an efficient way to generate a model for describing the complex spectra.

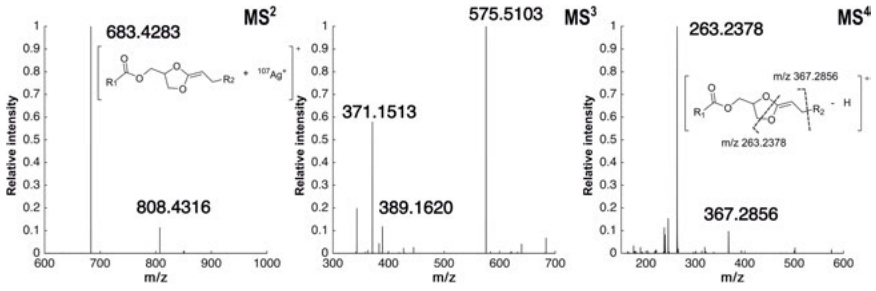

Figure 4.3. MS^n transitions for PC 18:1_16:0. At the MS^2 loss of head group is the base peak product ion (*m/z* 683.4283). MS^3 of the precursor at *m/z* 683.4238 shows a loss of AgH as the main product ion (*m/z* 575.5103). Structurally informative product ions are then fromed at MS^4 through cleavages of the dioxolane ring. Adapted with permission from Lillja, J.; Lanekoff, I. *Analytical and Bioanalytical Chemistry* **2022**, *414*, 7473–7482 ©Author(s) 2022

$$Y = \beta X + \epsilon \tag{4.1}$$

In **paper II** the product ions of silver adducts of glycerolipids were studied in MS^n and shown in Figure 4.3. The head group loss is expected in MS^2, however, the high abundance of PC-Headgroup at *m/z* 683.4283 is uncharacteristic of PC lipids but since the silver ion carries the charge instead of the phosphate headgroup. Interestingly, at the MS^3 level the most abundant product ion was detected at *m/z* 575.5103, corresponding to a neutral loss of AgH. The $[PC\text{-}headgroup\text{-}AgH]^+$ specie has been confirmed by cryogenic IR ion spectroscopy to be an allylic dioxolane product ion. [105] The fragmentation pathway was also studied with $cIMS^n$ spectrometry. It is known that IMS can separate the Ag^+ species of lipids, and it would therefore be of interest to know if the change in conformation is retained after neutral losses.[45] After losing the head group there is still a difference in conformation between the two isomers, as shown in Figure 4.4. However, after losing AgH the ions are inseparable, although shown to be a mixture of cis and trans allylic ions, $cIMS^3$ did not show any evidence of multiple conformational species.[105] The fragmentation of the allylic dioxolane forms product ions that are diagnostic for the sn position and quantitative.

Additionally, the dissociation pathway is not unique to PC species. Loss of head group, followed by AgH loss was observed for DAG, TAG, PE, and PS lipids. Similarly, it has been shown that a dioxolane ring structure is formed for these species as well.[107] Additionally, we performed $cIMS^n$ on PC 16:0_18:1 and PS 16:0_18:1 to validate that the same product ions are formed after head group loss. In Figure 4.4 the driftograms of the $[M\text{-}Headgroup{+}^{107}Ag]^+$ and $[M\text{-}Headgroup\text{-}^{107}AgH]^+$ shows that the product ions have the same drift times, meaning that the dissociation mechanism is the same and is general and applicable to other glycerolipids.

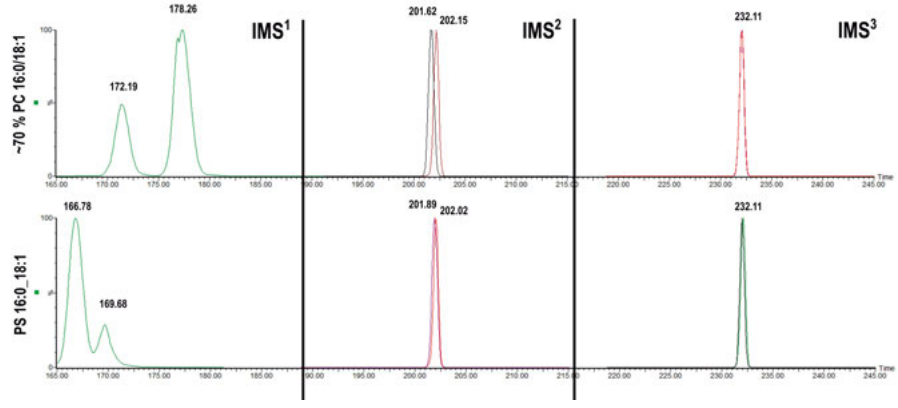

Figure 4.4. IMS^n of mixtures of the isomers PC 18:1_16:0 and PS 34:1 with the same IMS^n method showing separation at all stages except for the allylic dioxolane product ion. The PS lipid was not baseline separated in IMS^1, despite this, after dissociation of the head group the product ion has the same drift times as its PC counterpart showing that the dissociation pathway is independent of head group. Adapted with permission from Lillja, J.; Lanekoff, I. *Analytical and Bioanalytical Chemistry* **2022**, *414*, 7473–7482 ©Author(s) 2022

4.1.2 Quantification

Because of the diversity of lipids i.e. different head groups, acyl chain lengths, acyl chain positions, and degree of unsaturation, it is unreasonable to have one standard for each lipid in the sample. Because of the similarities in physicochemical properties within a lipid class, it is widely accepted to use one internal standard per lipid class. However, the method still needs careful planning because the degree of unsaturation and acyl chain length impacts the analytical response.[108]

The change in analytical response between two lipids of the same class but with different acyl chain lengths is in large due to ^{13}C isotopic effects.[109] This effect is illustrated in Figure 4.5 where more carbons increase the abundance of ^{13}C isotopologues, thus lowering the intensity of the monoisotopic peak. This effect can be removed by summing up all isotopologues in the quantitation, however, the low abundant isotopolouges are measured with comparatively low precision.[110] A more precise approach is, therefore, to correct for the theoretical isotopic abundance (assuming a natural ^{13}C distribution) according to Equation 4.2. The corrected intensity (I_x where x is the number of carbons in the analyte) for the analyte *a* and the standard *s* can then be used to calculate the concentration of C_a as shown in eq. 4.3. Thus enabling more accurate and precise quantification of phospholipids without the need for excessive internal standards.

$$I_x = I_x(1 + 0.0109x + \frac{0.0109^2 x(x-1)}{2} + ...) \tag{4.2}$$

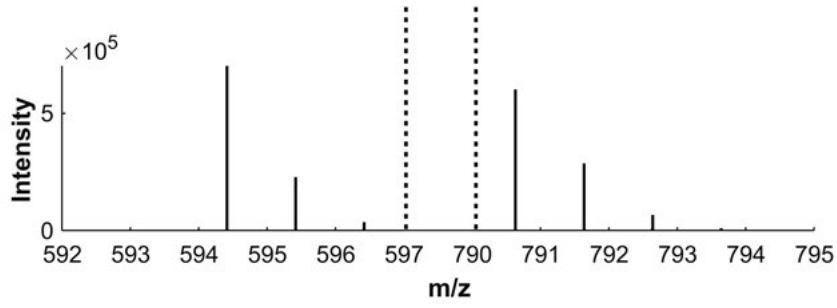

Figure 4.5. Simulated isotopic distribution of one million ions of protonated PC 22:0 and PC 36:0, showing the difference in monoisotopic response is due to different isotopologue distributions.

$$C_a = \frac{I_a}{I_s} C_s \tag{4.3}$$

The effects of ^{13}C are not limited to analytes that contain many carbons, but are also applicable in cases where ^{13}C labeled internal standards are used. This is illustrated in Figure 4.6 where a calibration curve of glucose $^{13}C_1$ was prepared gravimetrically using glucose $^{13}C_6$ as internal standard. The slope, or response factor, was estimated to be 0.9491 ($\pm$ 0.0033) which is close to the theoretical value 0.9478 calculated from Equation 4.2. This shows that the analytical response of ^{13}C labeled compounds may be equal to the non-labeled counterpart, and the experimental workflow can be simplified by calculating rather than measuring the response factor for accurate quantitative estimates.

Additionally, the ^{13}C effect also introduces a potential bias for relative quantification in *-omics* experiments using labeling techniques. In these kinds of experiments either samples are grown separately in labeled media, or isotopically labeled tags are used, and the ratio of a natural analyte is compared to a labeled one. This bias can be seen in the early works in proteomics using stable isotope labeling by amino acids in cell culture (SILAC), but has since been addressed in newer software tools.[111–113] Details like this are easily forgotten, and considering that it adds a potential bias of a few percent it might not be significant for most studies. However, as an analytical chemist, I think it is essential to know about these details and consciously either accept and acknowledge the bias or account for it.

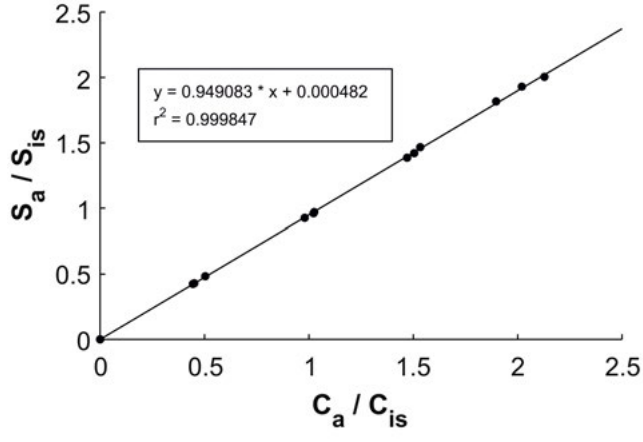

Figure 4.6. Calibration curve of glucose $^{13}C_1$ using $^{13}C_6$ as internal standard. The response (slope) matches the expected isotope correction

5. Results and discussion

The main goal for the methods I have developed is for the application of MSI, specifically, nano-DESI MSI, to reveal the distribution of analytes and different isomers in biological samples. There are several challenges addressed in this work, all of which regard speed, sensitivity, and throughput.

5.1 Spatial distribution of fatty acid isomers

Specific isomers of fatty acids are important in the function of the brain and have for example been shown to aid in the repair of ischemic stroke.[114] Because different isomers have various biological effects, it is of interest to visualize their distributions in tissue to unravel how they interact in a biological context.[115] There are currently a few available methods that are able to resolve isomeric species with mass spectrometry imaging, however, they require harsh instrumental or experimental modifications.[116–119] There is therefore a need for a simple method that requires little modifications to be done.

In **paper I** we therefore developed a method using MS^n of silver cationized fatty acids that was able to distinguish the isomeric pair oleic and vaccenic acid (FA 18:1 Δ9 and FA 18:1 Δ11, respectively). As discussed earlier, the product ions of these two isomers were identical in MS^2 and MS^3. However, the distributions of the two product ions was different at the MS^3 stage and were therefore modeled using a linear model.

The model was validated, and shown to be robust in biological matrices. This was done by spiking known amounts of oleic and vaccenic acid into complex samples and evaluating their ratio. In addition, the reproducibility was also high in complex matrices, with relative standard deviations in biological replicates below 10 %. When using silver cationization and measuring FA 18:1+^{107}Ag, an isobaric interference will be formed from FA 18:2+^{109}Ag. This isobaric interference needs at least 25 000 mass resolving power to be separated, which is attainable with modern high-resolution mass spectrometers. However, we instead opted to use monoisotopic silver to both remove this isobaric interference and to not *dilute* the signal into more mass channels. Although the method was robust and showed no spectral interferences, it was later realized that the data could be generated faster and potentially with more scans in the ion trap rather than the orbitrap used. The use of ion trap mass spectrometry was further pursued in **papers II and III**.

Because the model was shown to be resilient to biological matrices, the method was applied with nano-DESI MSI to visualize the distribution of isomeric fatty acids directly from tissue. In Figure 5.1 the distribution of oleic acid and vaccenic acid is shown as the mol % of oleic acid. There is a relative decrease of oleic acid in the hippocampus and an increase in the surrounding white matter. At the time, the detected ratio of oleic- to vaccenic acid was similar to previously reported values in the brain, and similar spatial distributions have since been reproduced with other methods.[117–119]

Although the fragmentation pattern of isomers of FA 18:2 follows the same pattern with water loss and CO loss, it was not pursued further because of the vast amount of potential isomers. It is also important to acknowledge that the strategy of modeling the product ion pattern of specific isomers is only valid when there are no other isomers present. In the case of mouse and rat tissue, it seems to be true.[117–119] However, newly developed methods have recently shown that more isomers, albeit in low amounts, are present in for example pancreatic cells.[120] Nonetheless, the ability to distinguish isomeric fatty acids and to visualize the distribution is still remarkable.

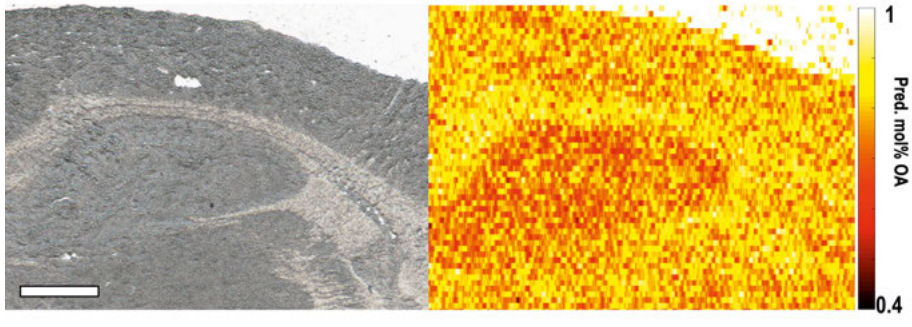

Figure 5.1. Optical and ion image of FA 18:1 in rat brain tissue, scale bar indicates 1 mm. The distribution of FA 18:1 Δ9 and FA 18:1 Δ11 is different depending on the region of tissue, with the lowest amount of FA 18:1 Δ9 in the hippocampus. Adapted with permission from Lillja, J. et al. *Journal of the American Society for Mass Spectrometry* **2020**, *31*, 2479–2487 ©2020 American Chemical Society

5.2 MSI of phospholipid isomers

Phospholipids can contain yet another form of isomerism, specifically *sn* isomerism of the acyl chains. The regiospecific positioning of the acyl chains has been shown to play a role in lipid-protein interaction and be altered in disease.[92, 121] Yet, separation and quantitative determination of regioisomeric phospholipids is hard. Therefore, in **paper II** a method to quantitatively determine the regioisomeric composition of phospholipids was developed using silver as an ionization reagent for application with mass spectrometry imaging. The addition of silver allowed for specific and sensitive MS^n analysis, where regioisomers could be quantitatively determined in MS^4. As discussed earlier, the silver ion attaches to the glycerolipid and allows the ion to keep the charge throughout the dissociation pathway. Specifically, at the MS^2 stage the phospholipid head group is lost, followed by a loss of AgH in MS^3, and finally a dioxolane ring cleavage in MS^4. Notably, the reduction of Ag^+ to AgH (determined by accurate mass) generates an allylic cation, that we show dissociates in a quantitative manner.[105] The high specificity of MS^4 allowed for the use of the lower resolution, but faster and more sensitive ion trap in the hybrid mass spectrometer at hand. Where in particular, spectral averaging could be carried out to increase the signal-to-noise without increasing the duty cycle too much. Because the available material is limited, and the spatial resolution is proportional to the duty cycle in nano-DESI MSI, a fast MS method is desirable.

The method was used to determine the *sn*-isomeric composition of PC 34:1 and PC 36:1 in a mouse brain tissue section using nano-DESI MSI. For PC 34:1, isomers of PC 18:1_16:0 was detected, and quantitative ion images are shown in Figure 5.2. The ion images of the precursor (Figure 5.2a) and its respective isomers (Figure 5.2c,d) look similar at first glance. However, by calculating the mol% of PC 16:0/18:1 a distinct distribution is shown throughout the tissue. Specifically, a relative increase of PC 16:0/18:1 can be seen in several regions of the tissue, including the white matter, thalamus, and within the hippocampus.

For the PC 36:1 species, two pairs of regioisomers were found, PC 18:1_18:0 and PC 20:1_16:0. In this case, the distribution was rather homogenous in MS^1 (Figure 5.3 a). However, similarly to previously published data, we show that this is mainly due to the isomer pairs of PC 18:1_18:0 (Figure 5.3b,c) whereas the less abundant isomer pair from PC 20:1_16:0 has a clear difference in its distribution.[122, 123] The less abundant isomer pairs of PC 20:1_16:0 show a clear lack of PC 20:1/16:0 in the white matter. It is often speculated that these distributions arise from phospholipase A2 (PLA_2) enzyme activity, however, because the PC 18:1_18:0 isomers do not distribute in a similar way it is more likely to be due to metabolic or structural activity in the region.[122]

Although it was shown in **paper I** that the dissociation of PC lipids also produces the necessary precursor for determining the double bond in the acyl

chain, this was not pursued in this study. The precursor generated for this was generated at the MS^3 stage, and the yield was different based on whether the 18:1 acyl chain was on the *sn*-1 or the *sn*-2 carbon. Thereby biasing the result to the double bonds in a specific chain. In conclusion, this newly developed strategy allowed for the visualization of phospholipid isomers in tissue. Thereby providing a tool for further detailed studies of lipid isomers in tissue.

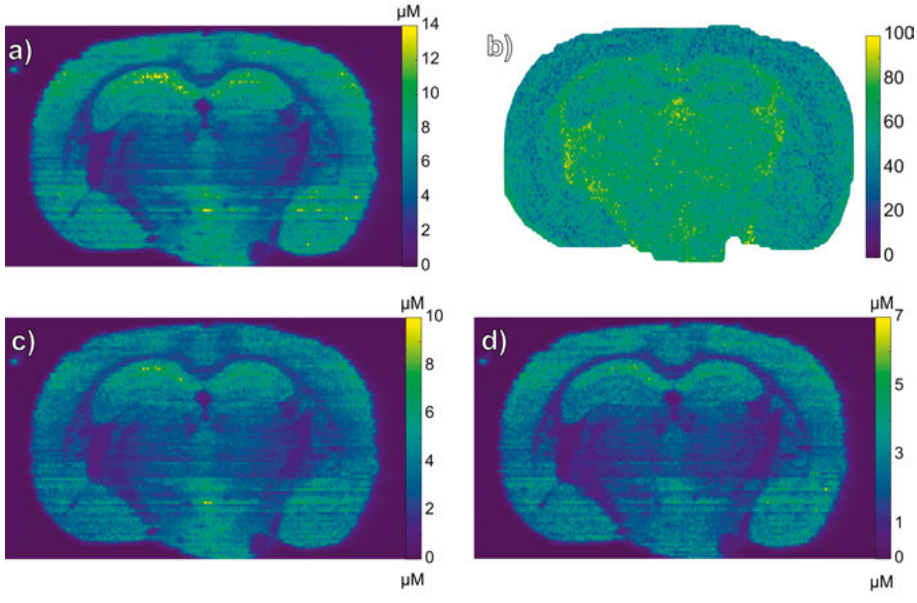

Figure 5.2. Ion images of PC 34:1 in mouse brain a) MS^1 b) molar fraction of PC 16:0/18:1 isomer c) quantitative ion image of PC PC 16:0/18:1 and d) quantitative ion image of PC PC 18:1/16:0. Although the isomers have a very similar distribution across the tissue, there is a distinct difference between the cortex and thalamus, there are also differences within the hippocampus. Adapted from Lillja, J.; Lanekoff, I. *Analytical and Bioanalytical Chemistry* **2022**, *414*, 7473–7482 ©2022 Author(s)

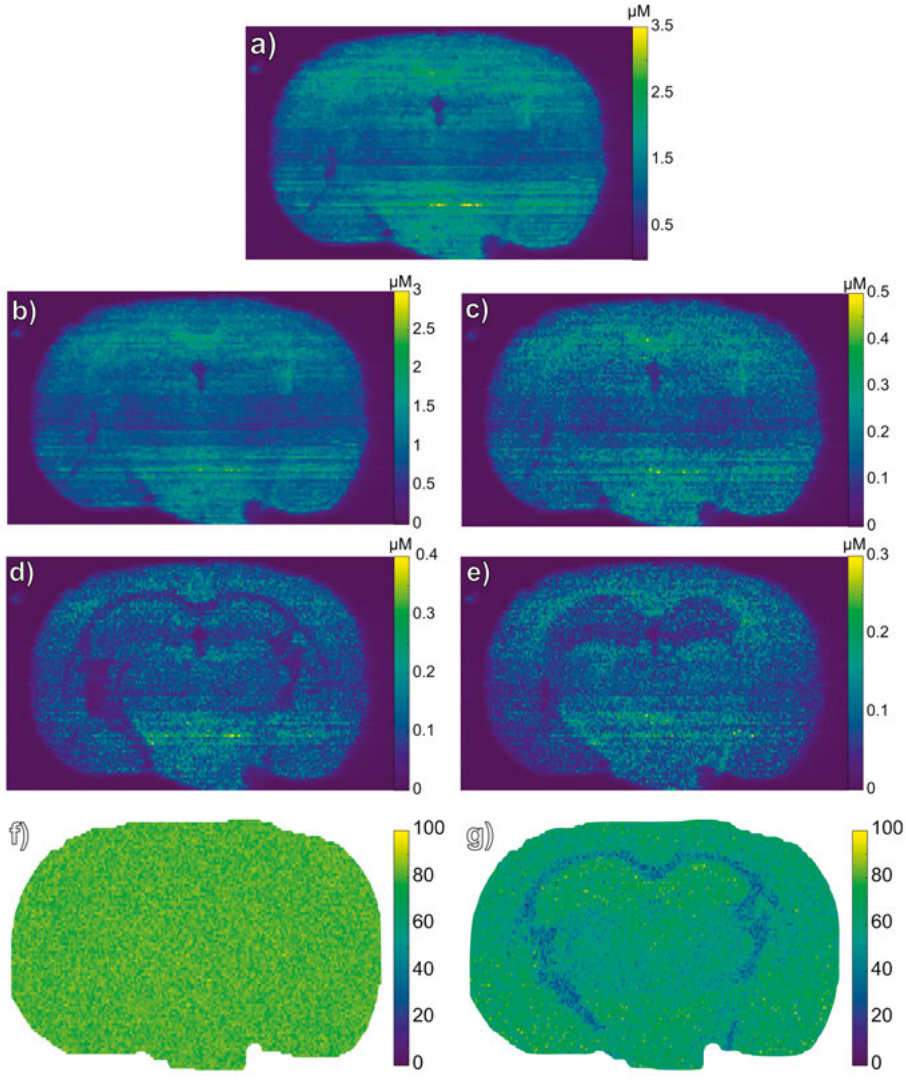

Figure 5.3. Quantitative ion images of PC 36:1 and the specific isomers detected. The ion image of 36:1 in MS^1 is shown in a), PC 18:1/18:0 from the MS^4 method in b), PC 18:0/18:1 from the MS^4 metod in c), PC 20:1/16:0 in d), PC 16:0/20:1 in e), and the mol% images of PC 18:1/18:0 and PC 20:1/16:0 respectively and f) and g). Adapted from Lillja, J.; Lanekoff, I. *Analytical and Bioanalytical Chemistry* **2022**, *414*, 7473–7482 ©2022 Author(s)

5.3 High-throughput MS^n MSI

Specificity in MSI is hard to get, and most methods rely on high mass resolving power alone. Throughout my work, I have strived to increase the specificity by incorporating MS^n scan events. However, by increasing the number of scan functions executed by the mass spectrometer, the duty cycle is increased. A

higher duty cycle for nano-DESI MSI results in either larger pixels or longer experimental runtime - both of which are undesirable.

With multi-detector mass spectrometers, such as IT/Orbitrap, faster ion trap scans can be acquired in parallel to the longer FTMS transient. However, methods for utilizing parallelized operation of the mass spectrometers are difficult to set up for MSI. Specifically, parallelized operations are typically allowed with data-dependant acquisition (DDA) methods, which makes it difficult to generate ion images from the data. Despite this, parallel ITMS/FTMS MSI has been shown with MSI for increased specificity.[124–126] However, to date, only a single ITMS event has been shown to be completed in parallel to the FTMS, thus limiting throughput.

In **paper III** we developed a method for highly parallelized ion trap MS^2 ($ITMS^2$) in parallel to the FTMS transient, to generate richer MSI data and methods to spatially correlate precursor/product ion(s). Notably, we were able to perform 28 MS^2 events in the ion trap in parallel to a 1024 ms FTMS transient. Thus vastly surpassing the number of parallel scans performed in MSI applications in previously published works.[124–126] This was realized by both a DDA method with a target list, and a method that executed targeted $ITMS^2$ from the same target list. The data structure generated by the DDA method was very complex. Specifically, the precursor ion needs to be detected in the survey scan to initiate the $ITMS^2$ scan, and the order of the scans is based on the intensity in the survey scan. This makes it so that each pixel may have a different number of $IMTS^2$ scans associated with it, while the scans can also come in a different order - making data processing very complex. We also developed a targeted $ITMS^2$ method, where each FTMS scan had the exact same data structure throughout the whole experiment. Despite the complications with the DDA method, we were able to untangle the data and generate ion images with both methods. Because the DDA method is dependent on detecting the precursor in the survey scan, it leaves holes where the intensity of the precursor is low Illustrated in Figure 5.4. The targeted parallel $ITMS^2$ method was therefore preferred to increase the richness of the data.

For example, the spatial distribution of precursor/product ion in both FTMS and $ITMS^2$ can be used to validate an annotation. In typical MSI applications, accurate mass is used for the annotation of features, which in the case of lipids only contains the sum formula (e.g. PC 38:4). By incorporating both $ITMS^2$ and the product ions' spatial distribution, more precise annotations can be done. In Figure 5.5 we show that the product ions from PC 38:4 both confirm the identity of the PC head group and have a product ion for a 20:4 acyl chain, with consistent spatial distribution to the precursor. The targeted PC 38:4 was thereby annotated as PC 20:4_18:0. Additionally, because the isolation of the precursor may include other ions than expected, the ion trap mass spectra may contain unexpected features. Here, the spatial distribution was used to link product ions with specific precursors in the isolation window. By combining

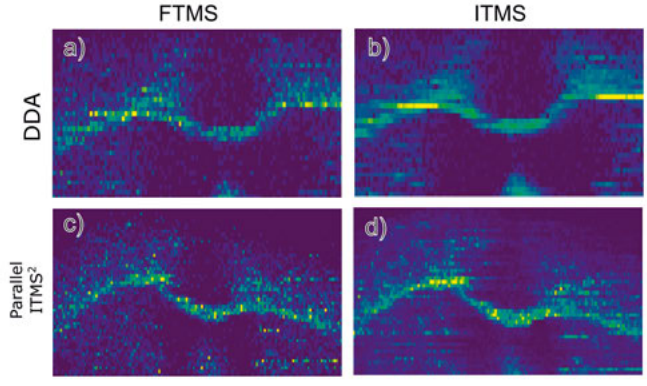

Figure 5.4. Ion images of PC 40:2 in a) FTMS with the DDA method b) $ITMS^2$ in ITMS with the DDA method c) FTMS with the targeted parallel method and d) $ITMS^2$ in ITMS with the targeted parallel method. Adapted from **paper III**

the accurate mass and the product ion distribution we were able to annotate a co-isolated specie at *m/z* 916.579 to HexCer 42:2;O2.

In addition to providing structural information about the targeted species, the signal-to-noise was higher for low abundant species in $ITMS^2$ compared to the FTMS. This was achieved because the $ITMS^2$ method was a targeted approach, increasing the dwell time for the selected precursor(s) in the ion trap. Specifically, the ion trap was allowed to isolate the precursors for up to 25 ms (in a 0.7 Th window), compared to injection times below 5 ms for the full scan between *m/z* 200-2000. The longer dwell times improved the ion statistics drastically, and are especially evident for low abundant species. An example of this is shown in Figure 5.6, where the ion images of PC 40:1 from the ITMS and FTMS are shown. The ion image from the ITMS has a greater dynamic range, as the signal in the FTMS creeps below the limit of detection in some regions. The increased dynamic range is shown in the histogram in Figure 5.6 where the detected quantities are shown in a histogram.

In conclusion, by performing $ITMS^2$ scans in parallel to the FTMS transient a richer data set can be acquired without increasing the overall duty cycle. The high degree of parallelization was made possible because of the high ion current generated from the nano-DESI ion source. The correlation between FTMS and $ITMS^2$ can be used to link precursor ions to specific product ions, thereby improving the annotation of unknown species by connecting the molecular formula derived from the accurate mass, to the product ions that localize to the same area(s). For low-abundant compounds, the increased dwell time allows for higher spectral quality, resulting in better ion images.

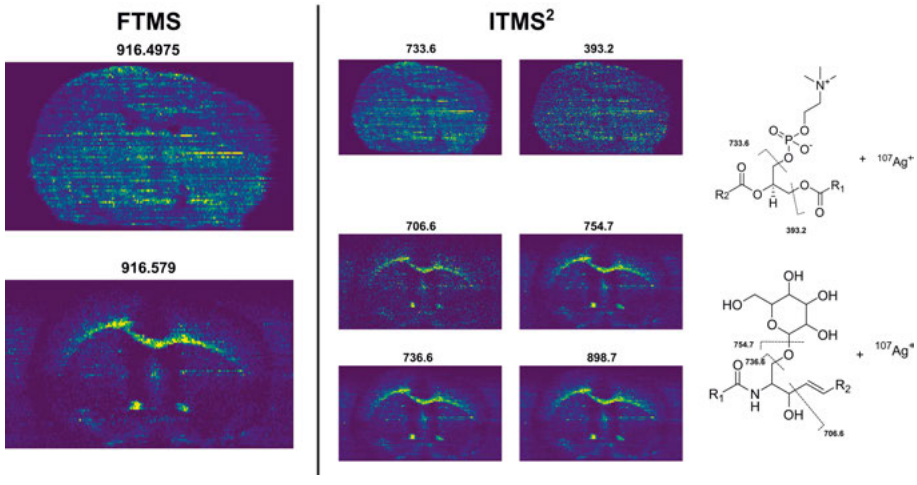

Figure 5.5. Ion image of PC 38:4 and co-isolated *m/z* 916.579 in MS^1 and $ITMS^2$. The product ions in $ITMS^2$ confirm the presence of the PC headgroup, which in conjunction with the accurate mass can be used to annotate the PC lipid. Additionally, the spatial location and the product ions show that the co-isolated species is a HexCer. Adapted from **paper III**

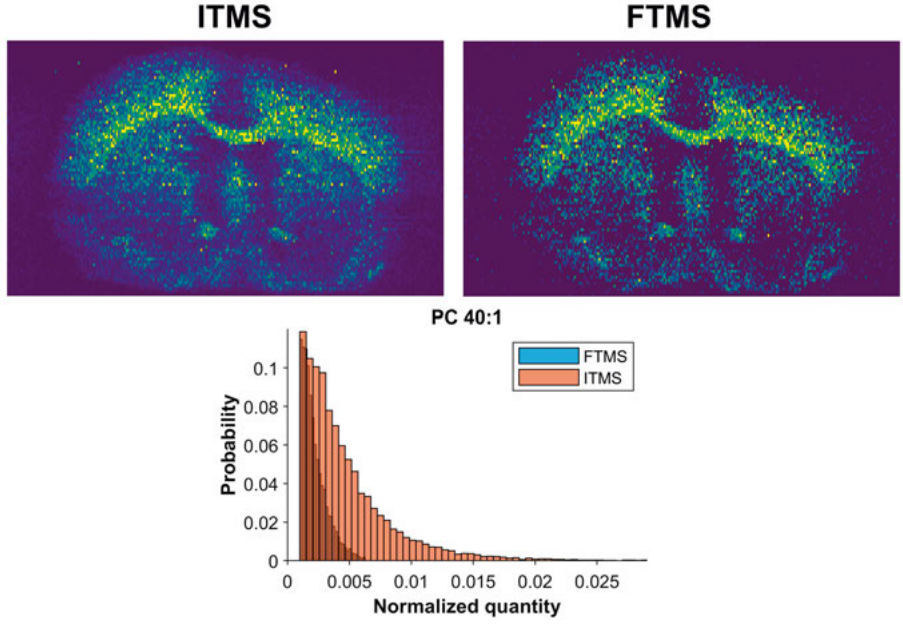

Figure 5.6. Ion image of PC 40:1 in ITMS (as [PC-Headgroup+^{107}Ag]$^+$) and FTMS (by accurate mass) normalized to the internal standard and scaled to the 99th percentile of pixel intensities. The normalized quantities between the two ion images are shown in the histogram. There was a greater dynamic range in the ITMS ion image. Adapted from **paper III**

5.4 Efficient data processing for MSI

With increasingly complex MSI experiments comes increasingly complex data processing workflows, and the need for solutions to process the data becomes almost as important as the experiments themselves. There are several commercial, free, and open-source software solutions for the processing of MSI data. [67–69] However, software with native support for nano-DESI MSI data sets are the commercially available PeakByPeak (Spectroswiss, Lausanne, Swizerland) and MSIQuickView.[56, 70] Additionally, as shown throughout this thesis, nano-DESI MSI experiments are capable of using arbitrarily complex MS^n experiments, which current software solutions can't process. Throughout my work, I have continuously developed a codebase in MATLAB to process the data from MSI experiments. In **paper IV** we decided to make a graphical user interface (GUI) named ion-to-image (i2i), shown in Figure 5.7, and share the project as open source to share the computational methods with the community.

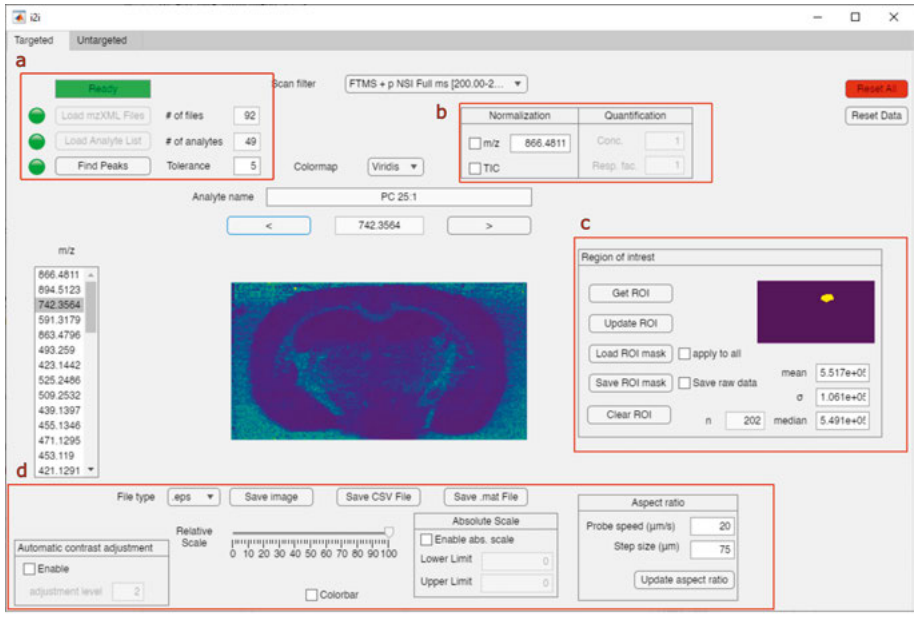

Figure 5.7. Graphical user interface of the i2i software application for processing of MSI data. The modules for a) file loading b) image normalization and quantification c) region of interest analysis and d) image adjustment is highlighted in red boxes. Reprinted with permission from Lillja, J. et al. *Analytical Chemistry* **2023**, *95*, 11589–11595 ©2023 Author(s)

I believe that the way you interact with the data has a major influence on what experiments you make. At the forefront of this is how fast you can load, and analyze the data. If for example, it would take 2h to load a data set, or to extract information from it you couldn't fully explore the data and likely

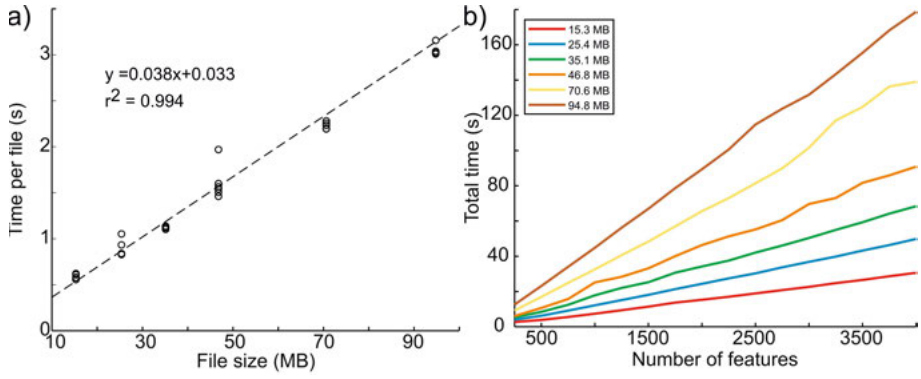

Figure 5.8. Performance metrics of the function used for a) file loading of a .mzML file as a function of size, and b) feature loading in the i2i application. Lillja, J. et al. *Analytical Chemistry* **2023**, *95*, 11589–11595 ©2023 Author(s)

miss interesting information. It was therefore of particular interest to the development of the program to i) allow for flexibility in experiment design and ii) speed of analysis.

This was achieved by using centroided .mzML data to reduce the file size and an in-house developed function to read the files in the computer. In this way, we could decide exactly what pieces of information should be loaded and thereby making it fast and customizable. Specifically, we store the *scan filter*, which contains a unique string that describes each MS experiment. In the i2i GUI there is a dropdown list that contains all unique *scan filters* from the experiment, which is used for the analysis of complex MS experiments, thereby allowing simple processing. Additionally, because in the .mzML conversion, the peaks are converted to centroids, the files get smaller than the original thereby making the file loading faster. Performance of the code published in **paper IV** for typical nano-DESI MSI data is shown in Figure 5.8 a), where the loading of a file is completed in seconds. Considering that a full image consists of about 40-100 individual line scans file loading is therefore done in minutes. Features and ion images are also generated fast, where it can be estimated from Figure 5.8 b) that it is completed in seconds to minutes depending on the number of features studied. The app, therefore, allows for fast and convenient data processing of nano-DESI MSI data.

Additionally, a high-resolution accurate mass data set is very information-dense, and typically only a small fraction of a data set is used in a study. This is because it can be time-consuming and computationally expensive to process the data set and still retain spatial information. However, there is a huge potential in being able to data mine the data. We, therefore, developed a way to perform non-targeted analysis. Contrary to published methods that utilize non-supervised models to stratify the image, in order to reduce the computational complexity, we developed a *supervised* model where data from a user-defined

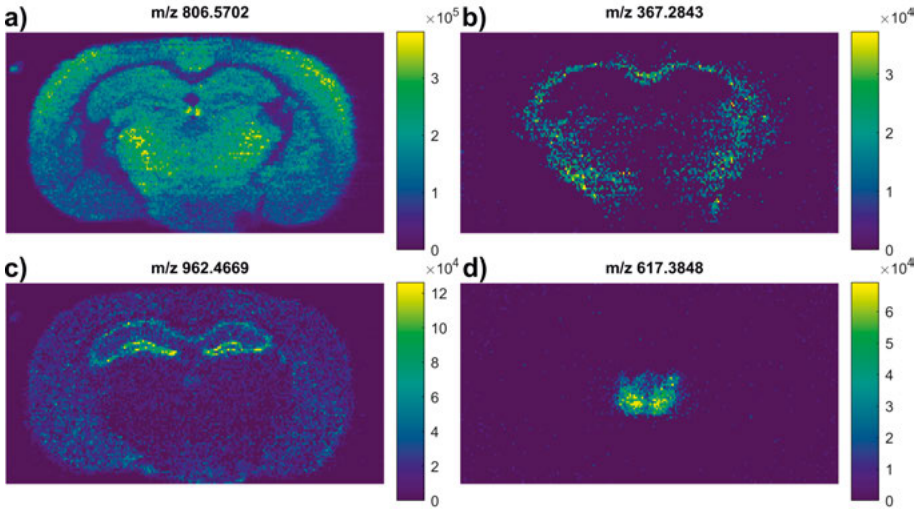

Figure 5.9. Examples of ion images generated by the non-targeted algorithm when comparing different regions at different intensity thresholds and detection frequency settings. A) Comparing the whole tissue region to glass with intensities 1E5-1E9 with detection frequencies between 50-100 %, b) Comparing the whole tissue region to glass with intensities 1E4-1E9 with detection frequencies between 10-30 %, c) Comparing the hippocampus to thalamus with intensities between 1E4-1E9 and detection frequencies between 10-100 %, and d) comparing thalamus to hippocampus with intensities between 1E4-1E9 and detection frequencies 10-100 %. Reprinted with permission from Lillja, J. et al. *Analytical Chemistry* **2023**, *95*, 11589–11595 ©2023 Author(s)

region is averaged and compared against another region.[127] In this way, we were able to perform spatially driven non-targeted analysis without extreme computational requirements. The effect of comparing different regions and threshold levels is shown in Figure 5.9, where features could be found fast and easily.

As of writing this, the application is widely used and much appreciated within the research group. The entire code base is open source, and free for anyone to download, use, and modify. The problems addressed with this program, mainly speed and usability, are bottlenecks in many research groups, which can now adapt this workflow.

6. Conclusions and future aspects

The field of mass spectrometry imaging is still developing, and improvements with regard to spatial resolution, specificity, and sensitivity are developed across many different labs. The flexibility offered by nano-DESI MSI has made it possible to show that i) silver is an excellent ionization reagent for lipidomic studies and ii) nano-DESI MSI is capable of generating enough ions for MS^n analysis. Specifically, in **papers I and II** silver ions were used as an ionization reagent to enable the study of novel dissociation pathways to distinguish isomeric species by MS^n. We show that isomers of both fatty acid and glycerolipids distribute differently in brain tissue, which to me indicates that biological processes are different in different regions. Relatively little is known regarding the processes that these isomers are involved in because of the analytical challenge of measuring them. However, in my opinion, the differential spatial distribution within a tissue section does indicate that biological processes/functions are different. Although not expanded upon in this thesis work, I believe that one interesting application would be to study isomer-specific lipid-protein interaction(s).[128]

In **paper III** I show, for the first time, highly multiplexed MSI experiments utilizing multiple detectors to improve the data quality in MSI. Because of the uniquely high ion yield, and sensitivity of electron multiplier detection, I was able to perform up to 28 targeted MS^2 experiments in parallel to a FTMS transient. This allowed for a combined targeted and non-targeted MSI workflow, where the structural identification was strengthened by both $ITMS^2$ data from the ion trap and accurate mass spectra from the Orbitrap mass analyzer. The Q-IT design of the instrument used in this study effectively makes up for one of the biggest drawbacks in ion trap mass spectrometry, namely ion statistics. By leveraging quadrupole isolation for isolation of precursor ions in the $ITMS^2$ scans a larger amount of ions are isolated compared to isolation in the ion trap. This results in more ions reaching the detector, and in addition to generating structural information, making better ion images of low abundant species in the process. Importantly, by not increasing the overall duty cycle, more information is generated without sacrificing time. This is important because, with continuous MSI techniques, the duty cycle of the mass spectrometer is proportional to the pixel size in the resulting ion image(s). It also emphasizes how well high-mass-resolution imaging data and low-mass-resolution imaging data work in tandem with each other. The spatial distribution can be leveraged to confirm which specific precursor the product ions are generated from, thus being an aid in deducing the structure of the analyte(s) from complex samples.

Additionally, although the primary purpose was to increase and validate the coverage of detected ions, the method could also be tweaked to improve the sampling of a few specific precursor ions and thus improve the quantitation. The capability of generating MSI data with extreme sensitivity and precision without abandoning broad FTMS scans has great implications for MSI workflows, especially as the spatial resolution increases and the samples get smaller, such as single cells.

The methods that I've developed revolve around getting more information from the mass spectrometer, which inevitably generates more complex and richer data sets. The work in **paper IV** addresses this by making an easy-to-use and fast data processing pipeline for both targeted and non-targeted MSI. Although the development of MSI software has been around for as long as MSI itself, there is not a one-size-fits-all for all techniques yet. As with any instrument or software, there is a fine balance between usability and customizability. Because most chemists are not avid programmers, it is important to supply a tool for performing the necessary data analysis, at the same time giving them the opportunity to dig deep and process manually using the source code. However, the data processing needs of tomorrow very well might not be the same as today, and more developments are likely needed. The open-source nature of the program hopefully encourages the use of it and further development of the codebase.

Populärvetenskaplig sammanfattning på svenska

Analytisk kemi är studiet om hur man kan använda olika strategier och methoder för att bestämma vad, hur mycket, och var ett ämne finns i ett prov. I den här avhandlingen diskuteras metodutveckling för att med avbildande masspektrometri studera lipider i biologisk vävnad. Masspektrometri är en analysteknik där massa till laddningsförhållandet av joner från ett prov bestäms. Genom att precist *väga* alla joner i ett prov så kan man säga vilka atomer som ingår i molekylen. På så vis kan man bestämma innehållet i ett komplext prov. Men, molekyler kan sättas ihop på olika vis så strategier för att bestämma precis vilken molekyl man har mätt måste utvecklas. Detta har jag gjort genom att *slå sönder* valda joner och kolla på mönstret av fragmenten som bildas, lite som att slå sönder porslin och lista ut om det var en mugg eller en tallrik. Genom att sedan modellera eller studera dessa mönster kan man precist säga vad det var för molekyl.

Dessa metoder har sedan används för studier i biologisk vävnad. Där har vi med hjälp av avbildande masspektrometri kunnat visualisera fördelningen av molekyler från olika platser i provet. Jag har genom att använda dessa metoder visat att fördelningen av lipider som är uppbyggda av samma atomer, men på olika sätt, är olika. Därmed kan man använda dessa verktyg för att studera hur biologiska system fungerar. Dessutom har jag utvecklat en metod för att göra flera mätningar parallelt, och på så vis öka mängden information man kan få i ett experiment utan att göra experimentet längre.

Ett problem som följer av metodutveckling för avbildande masspektrometri är hur man kan processa all data som man genererat, vilket oftast är flera gigabyte. Tekniken som vi använder för avbildande masspektrometri är relativt ny och mjukvara för att processa data genererat från den tekniken finns knappt. Vi har hemmagjorda lösningar för att processa data, och vi gjorde även ett grafiskt användargränssnitt med öppen källkod så att icke-experter kan processa data. Dessutom så utvecklade vi en strategi för att förenkla utforskande analyser, så att man kan använda så mycket av det genererade datat som möjligt.

Acknowledgements

First of all, I have to thank my main supervisor **Ingela**. I've been with you since my bachelor's project, and it has been great! I wasn't really interested in analytical chemistry before you showed me that it is more than making calibration curves, and I am very grateful for that. This work would also not have been possible without my first co-supervisor **Kyle**. I had a great time working with you and learning from you. All the best back home in Canada. **Daniel** my current co-supervisor, thanks for the support and helping me across the finish line.

Leonidas, I was lucky to get you here. Your presence has made this whole journey so much better with awesome office banter, disc-golf, and you even made me a football fan by making me go to Sirius games with you! **Catia**, always ready with a sassy comeback or roll your eyes over an obviously funny comment, I will miss you.

And of course, the newer students in the group, **Anastasia**, **Varun**, **Felix**, **Eszter**, **Lucie**, **Gabor**; you are great and will do great! Keep up the good times. Maybe the lab will be a bit tidier now when I am gone.

To the other PhD students, **Weifeng**, **Sandy**, **Mark**, **Ioanna**,**Sydney**, **Vladislav**, thanks for all the great lunches and interesting seminars. Soon you will write your own thesis, and I am sure it will be great.

The senior staff who has not only been good colleagues, but also always helpful with all their knowledge and expertise **Per**, **Kumari**, **Jonas**, **Jeff**, **Sara**, **Anna**, and the now retired **Marit** and **Jean**.

The post-docs at the department have also made it a good place, **Jonas**, **Aman**, **Alex**, **Stacey**, **Carina**, and **Fan**, good luck in your journeys!

Hilde, **Claudia**, **Malin**, **Neil**, **Marcus**, **Lina**, **Emma**, **Philipp**, **Mario**, I now know exactly what you also went through... Exhausting!

Eszter, now we've both done it! Thanks for being there at all times, I couldn't have done it without you. I love you I can't wait to see what the future holds for us!

Fredika, **Marcus**, jag lovar att visa **Lilly** massa experiment som inte är allt för stökiga! Om något år så får ni läsa den här boken för henne.

Mamma, **Pappa**, jag är fortfarande lika nyfiken som när jag var liten, tack för allt och erat oändliga tålamod!

References

(1) Griffiths, J. *Analytical Chemistry* **2008**, *80*, 5678–5683.

(2) Karas, M.; Bachmann, D.; Bahr, U.; Hillenkamp, F. *International Journal of Mass Spectrometry and Ion Processes* **1987**, *78*, 53–68.

(3) Whitehouse, C. M.; Dreyer, R. N.; Yamashita, M.; Fenn, J. B. *Analytical Chemistry* **1985**, *57*, 675–679.

(4) Kebarle, P.; Verkerk, U. H. *Mass spectrometry reviews* **2009**, 221–235.

(5) Olumee, Z.; Callahan, J. H.; Vertes, A. *The Journal of Physical Chemistry A* **1998**, *102*, 9154–9160.

(6) Iribarne, J. V.; Thomson, B. A. *The Journal of Chemical Physics* **2008**, *64*, 2287–2294.

(7) Dole, M.; Mack, L. L.; Hines, R. L.; Mobley, R. C.; Ferguson, L. D.; Alice, M. B. *The Journal of Chemical Physics* **2003**, *49*, 2240–2249.

(8) Konermann, L.; Ahadi, E.; Rodriguez, A. D.; Vahidi, S. *Analytical Chemistry* **2013**, *85*, 2–9.

(9) Schmidt, A.; Karas, M.; Dülcks, T. *Journal of the American Society for Mass Spectrometry* **2003**, *14*, 492–500.

(10) Morris, L. J. *Journal of Lipid Research* **1966**, *7*, 717–732.

(11) Jackson, A. U.; Shum, T.; Sokol, E.; Dill, A.; Cooks, R. G. *Analytical and Bioanalytical Chemistry* **2011**, *399*, 367–376.

(12) Duncan, K. D.; Fang, R.; Yuan, J.; Chu, R. K.; Dey, S. K.; Burnum-Johnson, K. E.; Lanekoff, I. *Analytical Chemistry* **2018**, *90*, 7246–7252.

(13) *CRC Handbook of Chemistry and Physics*, 103rd ed.; Internet Version 2022; CRC Press/Taylor & Francis: 2023.

(14) Paul, W. *Rev. Mod. Phys.* **1990**, *62*, 531–540.

(15) Schwartz, J. C.; Zhou, X.-G.; Bier, M. E. Method and apparatus of increasing dynamic range and sensitivity of a mass spectrometer, 1996.

(16) Murray, K. K. *Journal of the American Society for Mass Spectrometry* **2022**, *33*, 2342–2347.

(17) Douglas, D. J.; Frank, A. J.; Mao, D. *Mass Spectrometry Reviews* **2005**, *24*, 1–29.

(18) Koppenaal, D. W.; Barinaga, C. J.; Denton, M. B.; Sperline, R. P.; Hieftje, G. M.; Schilling, G. D.; Andrade, F. J.; Barnes IV, J. H. *Analytical Chemistry* **2005**, *77*.

(19) Pekar Second, T.; Blethrow, J. D.; Schwartz, J. C.; Merrihew, G. E.; MacCoss, M. J.; Swaney, D. L.; Russell, J. D.; Coon, J. J.; Zabrouskov, V. *Analytical Chemistry* **2009**, *81*, 7757–7765.

(20) Makarov, A. *Analytical Chemistry* **2000**, *72*, 1156–1162.

(21) Hu, Q.; Noll, R. J.; Li, H.; Makarov, A.; Hardman, M.; Graham Cooks, R. *Journal of Mass Spectrometry* **2005**, *40*, 430–443.

(22) Olsen, J. V.; Schwartz, J. C.; Griep-Raming, J.; Nielsen, M. L.; Damoc, E.; Denisov, E.; Lange, O.; Remes, P.; Taylor, D.; Splendore, M.; Wouters, E. R.; Senko, M.; Makarov, A.; Mann, M.; Horning, S. *Molecular & Cellular Proteomics* **2009**, *8*, 2759–2769.

(23) Michalski, A.; Damoc, E.; Hauschild, J. P.; Lange, O.; Wieghaus, A.; Makarov, A.; Nagaraj, N.; Cox, J.; Mann, M.; Horning, S. *Molecular and Cellular Proteomics* **2011**, *10*.

(24) Michalski, A.; Damoc, E.; Lange, O.; Denisov, E.; Nolting, D.; Müller, M.; Viner, R.; Schwartz, J.; Remes, P.; Belford, M.; Dunyach, J. J.; Cox, J.; Horning, S.; Mann, M.; Makarov, A. *Molecular and Cellular Proteomics* **2012**, *11*.

(25) Senko, M. W. et al. *Analytical Chemistry* **2013**, *85*, 11710–11714.

(26) Denisov, E.; Damoc, E.; Lange, O.; Makarov, A. *International Journal of Mass Spectrometry* **2012**, *325-327*, 80–85.

(27) Denisov, E.; Damoc, E.; Makarov, A. *International Journal of Mass Spectrometry* **2021**, *466*, 116607.

(28) Comisarow, M. B.; Marshall, A. G. *Canadian Journal of Chemistry* **1974**, *52*.

(29) Vining, B. A.; Bossio, R. E.; Marshall, A. G. *Analytical Chemistry* **1999**, *71*, 460–467.

(30) Lange, O.; Damoc, E.; Wieghaus, A.; Makarov, A. *International Journal of Mass Spectrometry* **2014**, *369*, 16–22.

(31) Gorshkov, M. V.; Fornelli, L.; Tsybin, Y. O. *Rapid Communications in Mass Spectrometry* **2012**, *26*, 1711–1717.

(32) Kaufmann, A.; Walker, S. *Rapid Communications in Mass Spectrometry* **2018**, *32*, 503–515.

(33) Bills, J. R.; Nagornov, K. O.; Kozhinov, A. N.; Williams, T. J.; Tsybin, Y. O.; Marcus, R. K. *Journal of the American Society for Mass Spectrometry* **2021**, *32*, 1224–1236.

(34) Sleno, L.; Volmer, D. A. *Journal of Mass Spectrometry* **2004**, *39*, 1091–1112.

(35) Cooks, R. G. *Journal of Mass Spectrometry* **1995**, *30*, 1215–1221.

(36) Tecklenburg, R. E. J.; Miller, M. N.; Russell, D. H. *Journal of the American Chemical Society* **1989**, *111*, 1161–1171.

(37) Zubarev, R. A.; Kelleher, N. L.; McLafferty, F. W. *Journal of the American Chemical Society* **1998**, *120*, 3265–3266.

(38) Syka, J. E. P.; Coon, J. J.; Schroeder, M. J.; Shabanowitz, J.; Hunt, D. F. *Proceedings of the National Academy of Sciences* **2004**, *101*, 9528–9533.

(39) Little, D. P.; Speir, J. P.; Senko, M. W.; O'Connor, P. B.; McLafferty, F. W. *Analytical Chemistry* **1994**, *66*, 2809–2815.

(40) McLuckey, S. A.; Goeringer, D. E. *Journal of Mass Spectrometry* **1997**, *32*, 461–474.

(41) Louris, J. N.; Cooks, R. G.; Syka, J. E.; Kelley, P. E.; Stafford, G. C.; Todd, J. F. *Analytical Chemistry* **1987**, *59*, 1677–1685.

(42) Ichou, F.; Schwarzenberg, A.; Lesage, D.; Alves, S.; Junot, C.; Machuron-Mandard, X.; Tabet, J.-C. *Journal of Mass Spectrometry* **2014**, *49*, 498–508.

(43) Giles, K.; Pringle, S. D.; Worthington, K. R.; Little, D.; Wildgoose, J. L.; Bateman, R. H. *Rapid Communications in Mass Spectrometry* **2004**, *18*, 2401–2414.

(44) Giles, K.; Ujma, J.; Wildgoose, J.; Pringle, S.; Richardson, K.; Langridge, D.; Green, M. *Analytical Chemistry* **2019**, *91*, 8564–8573.

(45) Maccarone, A. T.; Duldig, J.; Mitchell, T. W.; Blanksby, S. J.; Duchoslav, E.; Campbell, J. L. *Journal of Lipid Research* **2014**, *55*, 1668–1677.

(46) Castaing, R.; Slodzian, G. *J. Microscopie* **1962**, *1*, 395–410.

(47) Spengler, B.; Hubert, M.; Kaufmann, R. In *Proceedings of the 42nd annual conference on mass spectrometry and allied topics*, 1994, pp 1041–1041.

(48) Caprioli, R. M.; Farmer, T. B.; Gile, J. *Analytical Chemistry* **1997**, *69*, 4751–4760.

(49) Henderson, F.; Hart, P. J.; Pradillo, J. M.; Kassiou, M.; Christie, L.; Williams, K. J.; Boutin, H.; McMahon, A. *Rapid Communications in Mass Spectrometry* **2018**, *32*, 721–729.

(50) Miyamoto, S.; Hsu, C.-C.; Hamm, G.; Darshi, M.; Diamond-Stanic, M.; Declèves, A.-E.; Slater, L.; Pennathur, S.; Stauber, J.; Dorrestein, P. C.; Sharma, K. *EBioMedicine* **2016**, *7*, 121–134.

(51) Schwamborn, K.; Krieg, R. C.; Reska, M.; Jakse, G.; Knuechel, R.; Wellmann, A. *International Journal of Molecular Medicine* **2007**, *20*, 155–159.

(52) Cliff, B.; Lockyer, N.; Jungnickel, H.; Stephens, G.; Vickerman, J. C. *Rapid Communications in Mass Spectrometry* **2003**, *17*, 2163–2167.

(53) Römpp, A.; Guenther, S.; Schober, Y.; Schulz, O.; Takats, Z.; Kummer, W.; Spengler, B. *Angewandte Chemie International Edition* **2010**, *49*, 3834–3838.

(54) Takáts, Z.; Wiseman, J. M.; Gologan, B.; Cooks, R. G. *Science* **2004**, *306*, 471–473.

(55) Roach, P. J.; Laskin, J.; Laskin, A. *Analyst* **2010**, *135*, 2233–2236.

(56) Lanekoff, I.; Heath, B. S.; Liyu, A.; Thomas, M.; Carson, J. P.; Laskin, J. *Analytical Chemistry* **2012**, *84*, 8351–8356.

(57) Ellis, S. R.; Paine, M. R. L.; Eijkel, G. B.; Pauling, J. K.; Husen, P.; Jervelund, M. W.; Hermansson, M.; Ejsing, C. S.; Heeren, R. M. A. *Nature Methods* **2018**, *15*.

(58) Lanekoff, I.; Burnum-Johnson, K.; Thomas, M.; Short, J.; Carson, J. P.; Cha, J.; Dey, S. K.; Yang, P.; Prieto Conaway, M. C.; Laskin, J. *Analytical Chemistry* **2013**, *85*, 9596–9603.

(59) Lanekoff, I.; Thomas, M.; Carson, J. P.; Smith, J. N.; Timchalk, C.; Laskin, J. *Analytical Chemistry* **2013**, *85*, 882–889.

(60) *Analyst* **2014**, *139*, 3528–3532.

(61) Duncan, K. D.; Lanekoff, I. *Analytical Chemistry* **2018**, *90*, 2451–2455.

(62) Nguyen, S. N.; Sontag, R. L.; Carson, J. P.; Corley, R. A.; Ansong, C.; Laskin, J. *Journal of the American Society for Mass Spectrometry* **2018**, *29*, 316–322.

(63) Lanekoff, I.; Thomas, M.; Laskin, J. *Analytical Chemistry* **2014**, *86*, 1872–1880.

(64) Bergman, H. M.; Lundin, E.; Andersson, M.; Lanekoff, I. *Analyst* **2016**, *141*, 3686–3695.

(65) Cooper, H. J.; Hale, O. J. *Analytical Chemistry* **2021**, *93*, 4619–4627.

(66) Duncan, K. D.; Bergman, H.-M.; Lanekoff, I. *Analyst* **2017**, *142*, 3424–3431.

(67) Källback, P.; Nilsson, A.; Shariatgorji, M.; Andrén, P. E. *Analytical Chemistry* **2016**, *88*, 4346–4353.

(68) Race, A. M.; Palmer, A. D.; Dexter, A.; Steven, R. T.; Styles, I. B.; Bunch, J. *Analytical Chemistry* **2016**, *88*, 9451–9458.

(69) Bokhart, M. T.; Nazari, M.; Garrard, K. P.; Muddiman, D. C. *Journal of the American Society for Mass Spectrometry* **2018**, *29*, 8–16.

(70) Thomas, M.; Heath, B. S.; Laskin, J.; Li, D.; Liu, E.; Hui, K.; Kuprat, A. P.; Kleese van Dam, K.; Carson, J. P. In *2012 Annual International Conference of the IEEE Engineering in Medicine and Biology Society*, 2012, pp 5545–5548.

(71) Lillja, J.; Duncan, K. D.; Lanekoff, I. *Analytical Chemistry* **2023**, *95*, 11589–11595.

(72) Qi, Y.; O'Connor, P. B. *Mass Spectrometry Reviews* **2014**, *33*, 333–352.

(73) Römpp, A.; Schramm, T.; Hester, A.; Klinkert, I.; Both, J.-P.; Heeren, R. M. A.; Stöckli, M.; Spengler, B. In *Data Mining in Proteomics: From Standards to Applications*, Hamacher, M., Eisenacher, M., Stephan, C., Eds.; Humana Press: Totowa, NJ, 2011, pp 205–224.

(74) Tsybin, Y. O.; Nagornov, K. O.; Kozhinov, A. N. In *Fundamentals and Applications of Fourier Transform Mass Spectrometry*, Kanawati, B., Schmitt-Kopplin, P., Eds.; Elsevier: 2019, pp 113–132.

(75) Deutsch, E. W. In *Proteome Bioinformatics*, Hubbard, S. J., Jones, A. R., Eds.; Humana Press: Totowa, NJ, 2010, pp 319–331.

(76) Smets, T.; Verbeeck, N.; Claesen, M.; Asperger, A.; Griffioen, G.; Tousseyn, T.; Waelput, W.; Waelkens, E.; De Moor, B. *Analytical Chemistry* **2019**, *91*, 5706–5714.

(77) Han, X. *Nature Reviews Endocrinology* **2016**, *12*, 668–679.

(78) Johnson, C. H.; Ivanisevic, J.; Siuzdak, G. *Nature Reviews Molecular Cell Biology* **2016**, *17*, 451–459.

(79) Holčapek, M.; Liebisch, G.; Ekroos, K. *Analytical Chemistry* **2018**, *90*, 4249–4257.

(80) Lee, H.-C.; Yokomizo, T. *Biochemical and Biophysical Research Communications* **2018**, *504*, 576–581.

(81) Vallianatou, T.; Lin, W.; Bèchet, N. B.; Correia, M. S.; Shanbhag, N. C.; Lundgaard, I.; Globisch, D. *Journal of Cerebral Blood Flow & Metabolism* **2021**, *41*, 3324–3338.

(82) Piehowski, P. D.; Zhu, Y.; Bramer, L. M.; Stratton, K. G.; Zhao, R.; Orton, D. J.; Moore, R. J.; Yuan, J.; Mitchell, H. D.; Gao, Y.; Webb-Robertson, B. J. M.; Dey, S. K.; Kelly, R. T.; Burnum-Johnson, K. E. *Nature Communications* **2020**, *11*, 1–12.

(83) Dewez, F.; Oejten, J.; Henkel, C.; Hebeler, R.; Neuweger, H.; De Pauw, E.; Heeren, R. M. A.; Balluff, B. *PROTEOMICS* **2020**, *20*, 1900369.

(84) Harayama, T.; Riezman, H. *Nature Reviews Molecular Cell Biology* **2018**, *19*, 281–296.

(85) Liebisch, G.; Vizcaíno, J. A.; Köfeler, H.; Trötzmüller, M.; Griffiths, W. J.; Schmitz, G.; Spener, F.; Wakelam, M. J. *Journal of Lipid Research* **2013**, *54*, 1523–1530.

(86) Astudillo, A. M.; Meana, C.; Guijas, C.; Pereira, L.; Lebrero, P.; Balboa, M. A.; Balsinde, J. *Journal of Lipid Research* **2018**, *59*, 237–249.

(87) Kyle, J. E. et al. *Analyst* **2016**, *141*, 1649–1659.

(88) Han, X.; Gross, R. W. *Journal of Lipid Research* **2003**, *44*, 1071–1079.

(89) Nakanishi, H.; Iida, Y.; Shimizu, T.; Taguchi, R. *The Journal of Biochemistry* **2010**, *147*, 245–256.

(90) Zheng, X.; Smith, R. D.; Baker, E. S. *Current Opinion in Chemical Biology* **2018**, *42*, 111–118.

(91) Höring, M.; Ekroos, K.; Baker, P. R.; Connell, L.; Stadler, S. C.; Burkhardt, R.; Liebisch, G. *Analytical Chemistry* **2020**, *92*, 10966–10970.

(92) Cao, W.; Cheng, S.; Yang, J.; Feng, J.; Zhang, W.; Li, Z.; Chen, Q.; Xia, Y.; Ouyang, Z.; Ma, X. *Nature Communications* **2020**, *11*, 1–11.

(93) Young, R. S.; Bowman, A. P.; Tousignant, K. D.; Poad, B. L.; Gunter, J. H.; Philp, L. K.; Nelson, C. C.; Ellis, S. R.; Heeren, R. M.; Sadowski, M. C.; Blanksby, S. J. *Journal of Lipid Research* **2022**, *63*, 100223.

(94) Thomas, M. C.; Mitchell, T. W.; Harman, D. G.; Deeley, J. M.; Nealon, J. R.; Blanksby, S. J. *Analytical Chemistry* **2008**, *80*, 303–311.

(95) Williams, P. E.; Klein, D. R.; Greer, S. M.; Brodbelt, J. S. *Journal of the American Chemical Society* **2017**, *139*, 15681–15690.

(96) Ma, X.; Xia, Y. *Angewandte Chemie - International Edition* **2014**, *53*, 2592–2596.

(97) Klein, D. R.; Feider, C. L.; Garza, K. Y.; Lin, J. Q.; Eberlin, L. S.; Brodbelt, J. S. *Analytical Chemistry* **2018**, *90*, 10100–10104.

(98) Born, M.-E. N.; Prentice, B. M. *International Journal of Mass Spectrometry* **2020**, *452*, 116338.

(99) Paine, M. R.; Poad, B. L.; Eijkel, G. B.; Marshall, D. L.; Blanksby, S. J.; Heeren, R. M.; Ellis, S. R. *Angewandte Chemie - International Edition* **2018**, *57*, 10530–10534.

(100) Specker, J. T.; Van Orden, S. L.; Ridgeway, M. E.; Prentice, B. M. *Analytical Chemistry* **2020**, *92*, 13192–13201.

(101) Bednařík, A.; Bölsker, S.; Soltwisch, J.; Dreisewerd, K. *Angewandte Chemie - International Edition* **2018**, *57*, 12092–12096.

(102) Unsihuay, D.; Su, P.; Hu, H.; Qiu, J.; Kuang, S.; Li, Y.; Sun, X.; Dey, S. K.; Laskin, J. *Angewandte Chemie International Edition* **2021**.

(103) Lillja, J.; Duncan, K. D.; Lanekoff, I. *Journal of the American Society for Mass Spectrometry* **2020**, *31*, 2479–2487.

(104) Draper, N. R., *Applied regression analysis*, Third edition.; Wiley Series in Probability and Statistics; John Wiley & Sons, Inc.: Hoboken, New Jersey, 1998.

(105) Kirschbaum, C.; Greis, K.; Gewinner, S.; Schöllkopf, W.; Meijer, G.; von Helden, G.; Pagel, K. *Analytical and Bioanalytical Chemistry* **2022**.

(106) Lillja, J.; Lanekoff, I. *Analytical and Bioanalytical Chemistry* **2022**, *414*, 7473–7482.

(107) Kirschbaum, C.; Greis, K.; Polewski, L.; Gewinner, S.; Schöllkopf, W.; Meijer, G.; von Helden, G.; Pagel, K. *Journal of the American Chemical Society* **2021**, *143*, 14827–14834.

(108) Koivusalo, M.; Haimi, P.; Heikinheimo, L.; Kostiainen, R.; Somerharju, P. *Journal of Lipid Research* **2001**, *42*, 663–672.

(109) Han, X.; Gross, R. W. *Analytical Biochemistry* **2001**, *295*, 88–100.

(110) Yang, K.; Han, X. *Metabolites* **2011**, *1*, 21–40.

(111) Ong, S. E.; Kratchmarova, I.; Mann, M. *Journal of Proteome Research* **2003**, *2*, 173–181.

(112) Blagoev, B.; Kratchmarova, I.; Ong, S. E.; Nielsen, M.; Foster, L. J.; Mann, M. *Nature Biotechnology* **2003**, *21*, 315–318.

(113) Cox, J.; Mann, M. *Nature Biotechnology* **2008**, *26*, 1367–1372.

(114) Song, J.; Kim, Y.-S.; Lee, D. H.; Lee, S. H.; Park, H. J.; Lee, D.; Kim, H. *Scientific Reports* **2019**, *9*.

(115) Zhang, H.; Xu, M.; Shi, X.; Liu, Y.; Li, Z.; Jagodinsky, J. C.; Ma, M.; Welham, N. V.; Morris, Z. S.; Li, L. *Chemical Science* **2021**, *12*, 8115–8122.

(116) Feider, C. L.; MacIas, L. A.; Brodbelt, J. S.; Eberlin, L. S. *Analytical Chemistry* **2020**, *92*, 8386–8395.

(117) Ma, X.; Chong, L.; Tian, R.; Shi, R.; Hu, T. Y.; Ouyang, Z.; Xia, Y. *Proceedings of the National Academy of Sciences* **2016**, *113*, 2573–2578.

(118) Tang, F.; Guo, C.; Ma, X.; Zhang, J.; Su, Y.; Tian, R.; Shi, R.; Xia, Y.; Wang, X.; Ouyang, Z. *Analytical Chemistry* **2018**, *90*, 5612–5619.

(119) Koktavá, M.; Valášek, J.; Bezdeková, D.; Prysiazhnyi, V.; Adamová, B.; Beneš, P.; Navrátilová, J.; Hendrych, M.; Vlček, P.; Preisler, J.; Bednařík, A. *Analytical Chemistry* **2022**, *94*, 8928–8936.

(120) Zhang, H.; Xu, M.; Shi, X.; Liu, Y.; Li, Z.; Jagodinsky, J. C.; Ma, M.; Welham, N. V.; Morris, Z. S.; Li, L. *Chemical Science* **2021**, *12*, 8115–8122.

(121) Mousson, F.; Coïc, Y.-M.; Baleux, F.; Beswick, V.; Sanson, A.; Neumann, J.-M. *Biochemistry* **2002**, *41*, 13611–13616.

(122) Paine, M. R.; Poad, B. L.; Eijkel, G. B.; Marshall, D. L.; Blanksby, S. J.; Heeren, R. M.; Ellis, S. R. *Angewandte Chemie - International Edition* **2018**, *57*, 10530–10534.

(123) Claes, B. S. R.; Bowman, A. P.; Poad, B. L. J.; Young, R. S. E.; Heeren, R. M. A.; Blanksby, S. J.; Ellis, S. R. *Analytical Chemistry* **2021**, *93*, 9826–9834.

(124) Perdian, D. C.; Lee, Y. J. *Analytical Chemistry* **2010**, *82*, 9393–9400.

(125) OuYang, C.; Chen, B.; Li, L. *Journal of the American Society for Mass Spectrometry* **2015**, *26*, 1992–2001.

(126) Ellis, S. R.; Paine, M. R. L.; Eijkel, G. B.; Pauling, J. K.; Husen, P.; Jervelund, M. W.; Hermansson, M.; Ejsing, C. S.; Heeren, R. M. A. *Nature Methods* **2018**, *15*.

(127) Verbeeck, N.; Caprioli, R. M.; Van de Plas, R. *Mass Spectrometry Reviews* **2020**, *39*, 245–291.

(128) Corradi, V.; Sejdiu, B. I.; Mesa-Galloso, H.; Abdizadeh, H.; Noskov, S. Y.; Marrink, S. J.; Tieleman, D. P. *Chemical Reviews* **2019**, *119*, 5775–5848.

Acta Universitatis Upsaliensis

Digital Comprehensive Summaries of Uppsala Dissertations from the Faculty of Science and Technology 2293

Editor: The Dean of the Faculty of Science and Technology

A doctoral dissertation from the Faculty of Science and Technology, Uppsala University, is usually a summary of a number of papers. A few copies of the complete dissertation are kept at major Swedish research libraries, while the summary alone is distributed internationally through the series Digital Comprehensive Summaries of Uppsala Dissertations from the Faculty of Science and Technology. (Prior to January, 2005, the series was published under the title "Comprehensive Summaries of Uppsala Dissertations from the Faculty of Science and Technology".)

Distribution: publications.uu.se
urn:nbn:se:uu:diva-509042

ACTA UNIVERSITATIS
UPSALIENSIS
2023